



LUND
UNIVERSITY

Master of Science Thesis

Characteristics of a Flattening Filter Free Photon Beam – Measurements and Monte Carlo Simulations

Mårten Lind

Supervisors:

¹Elinore Wieslander

¹Tommy Knöös

²Brendan McClean

²Patrick McCavana

The work has been performed at:

¹Radiation Physics, Lund University Hospital, Lund, Sweden
and

²The Department of Radiation Physics,
St. Luke's Hospital, Dublin, Ireland

Medical Radiation Physics
Clinical Sciences, Lund
Lund University, 2008

Abstract

Introduction: In conventional medical linear accelerators, the flattening filter is introduced in the photon beam line to provide a uniform lateral dose profile at a specified depth in water. For some radiotherapy treatments, e.g. intensity modulated radiotherapy, a flat radiation field is not necessary and the flattening filter could be removed. Several studies have shown that removal of the filter improves some properties of the photon beam, which could be beneficial for these treatments. The purpose of this work was to characterise the photon beam from a flattening-filter free linear accelerator by both measurements and Monte Carlo (MC) simulations.

Material and Methods: An Elekta *Precise* medical linear accelerator was modified for flattening-filter free beam delivery, using the initial electron beam energy of a conventional 6 MV beam. The flattening filter was replaced with a copper plate provided by Elekta. The MC model of the flattening-filter free accelerator was validated by comparing calculated depth-dose curves and profiles with measurements. The investigated characteristics of this new beam included depth-dose curves, lateral dose profiles, output factors, beam quality and evaluation of both photon fluence and the origin of photons.

Results: The results showed an increased dose output per initial electron at the central axis of 1.75 and a reduced amount of scattered photons from the accelerator head of 12.7 ± 0.6 % and hence a reduced variation of output factors for different field sizes was found. The photon spectrum of the unflattened beam was softer compared to a conventional beam and did not vary significantly off-axis. As a consequence, the shape of the dose profiles varied less with depth in water for the flattening filter free beam.

Conclusions: A MC model of a flattening-filter free accelerator has been developed and verified. Measurements and computer simulations have shown that this new beam possesses several advantages, especially for the delivery of intensity-modulated radiotherapy. It can also be expected that more accurate dose calculations would be possible since corrections in the treatment planning systems, e.g. for scattered radiation and off-axis softening, are less important.

Contents

1	INTRODUCTION	1
1.1	PURPOSE	1
1.2	BACKGROUND.....	1
1.3	TREATMENTS WITHOUT THE FLATTENING FILTER	2
1.3.1	<i>Portal Imaging</i>	5
1.3.2	<i>Tumour Dose Enhancement with High Z-material</i>	6
1.4	TREATMENT PLANNING SYSTEM	6
1.5	RADIATION SAFETY	7
2	MATERIAL AND METHODS.....	8
2.1	THE ACCELERATOR.....	8
2.1.1	<i>Filter Configuration</i>	8
2.1.2	<i>Beam Set-up</i>	9
2.2	EXPERIMENTAL DATA COLLECTION	9
2.2.1	<i>Central-axis Depth-dose</i>	10
2.2.2	<i>Profiles</i>	10
2.2.2.1	<i>Penumbral Width</i>	11
2.2.2.2	<i>Dose Profile Variation with Respect to Depth in Water</i>	11
2.2.3	<i>Output Factors in Air</i>	12
2.2.4	<i>Output Factors in Water</i>	13
2.2.5	<i>Beam Quality</i>	13
2.3	MONTE CARLO SIMULATIONS	14
2.3.1	<i>General Description of the Monte Carlo Simulation Technique</i>	14
2.3.2	<i>Accelerator Simulation with BEAMnrc</i>	14
2.3.3	<i>PEGS4</i>	16
2.3.4	<i>Variance Reduction Methods</i>	16
2.3.4.1	<i>Transport Cutoff Energies</i>	17
2.3.4.2	<i>Secondary Particles Production Thresholds</i>	17
2.3.4.3	<i>Range Rejection</i>	17
2.3.4.4	<i>Bremsstrahlung Splitting and Russian Roulette</i>	18
2.3.5	<i>Phase Space Files</i>	19
2.3.6	<i>LATCH</i>	19
2.3.7	<i>Phantom Simulation with DOSXYZnrc</i>	19
2.4	DATA CALCULATIONS WITH THE MONTE CARLO METHOD.....	20
2.4.1	<i>Parameter Settings</i>	20
2.4.2	<i>Benchmark Calculations</i>	20
2.4.3	<i>Calculation of Lateral Dose Profiles and Depth-dose Curves</i>	22
2.4.4	<i>Phase Space Analysis</i>	22
2.4.4.1	<i>Investigated Beam Properties</i>	22
2.4.4.2	<i>Half-value Layer Calculations</i>	23
2.4.4.2.1	<i>Evaluation of Phase Space for HVL</i>	23
3	RESULTS AND DISCUSSION	25
3.1	MEASUREMENTS	25
3.1.1	<i>Lateral Dose Profiles</i>	25
3.1.1.1	<i>Dose Profile Variation with Respect to Depth in Water</i>	25
3.1.1.2	<i>Penumbral Width</i>	28
3.1.2	<i>Depth-dose Curves</i>	28
3.1.3	<i>Output Factors in Air</i>	29
3.1.4	<i>Output Factors in Water</i>	32
3.1.5	<i>Beam Quality</i>	32

3.2 MONTE CARLO SIMULATIONS	33
3.2.1 <i>Benchmarking</i>	33
3.2.2 <i>Photon Fluence</i>	35
3.2.3 <i>Dose Output</i>	38
3.2.4 <i>Angular distribution</i>	39
3.2.5 <i>Photon Origin</i>	40
3.2.6 <i>Variation of HVL with Off-Axis Angle</i>	41
4 CONCLUSIONS AND FUTURE WORK.....	43
ACKNOWLEDGEMENTS	44
REFERENCES	45
APPENDIX	49

1 Introduction

1.1 Purpose

When a new type of radiotherapy treatment, as in this case a flattening filter free beam from a conventional accelerator, is being introduced, it is of great value to know the properties of this new beam and how it relates to a conventional radiotherapy beam. The purpose of this study was to investigate the properties of a flattening filter free beam generated by an Elekta Precise accelerator, by both measurements and by developing a computer model of the accelerator in order to conduct Monte Carlo (MC) simulations of this new beam.

1.2 Background

In external radiotherapy, the x-ray treatment fields are usually delivered by a medical linear accelerator (linac). Electrons are accelerated, inside a waveguide, up to the desired treatment energy, approx. 6 MeV for a 6 MV beam. The beam is then led by bending magnets to hit a target and x-rays are produced by the bremsstrahlung production process. These high-energy x-rays are forward peaked with the highest intensity in the direction parallel to the incident electron beam. To be useful for conventional radiotherapy the treatment fields has to be uniform (Metcalf, et al., 2004). This ‘beam flatness’ is achieved by the introduction of a flattening filter in the beam line. The flattening filter is a cone-shaped piece of metal that absorb more radiation at its centre than at the periphery, thus creating a field of uniform intensity at a specified depth of a homogenous media, for example at 10 cm depth with a *source-to-surface distance* (SSD) of 90 cm. At other depths the beam will not be uniform, especially not at the field edges of larger fields. This is due to the different magnitude of the hardening effect at the centre of the flattening filter to a position off the central axis, i.e. the beam has a softer energy spectra the further away from the central axis you go (Lee, 1997, Lovelock, et al., 1995). In order to deliver a specified treatment field, a set of movable collimators defines the photon field. In Figure 1.1, a schematic illustration of the accelerator head of an Elekta Precise is shown.

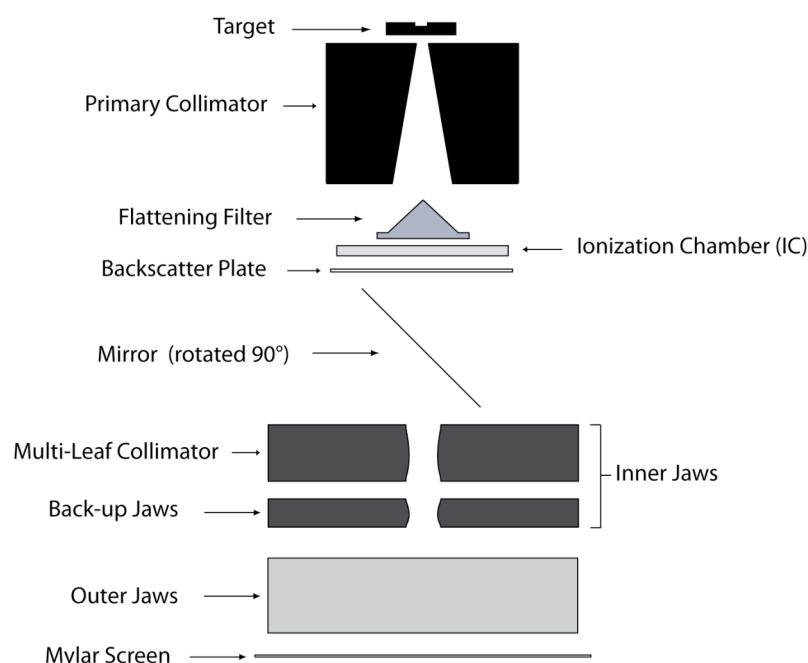


Figure 1.1 Simplified cross section of the components in an Elekta Precise linac head for the production of a 6 MV photon beam (not to scale).

1.3 Treatments without the Flattening Filter

Although the flattening filter is a necessity for many of the treatments delivered today it is, for some treatments, for example *intensity modulated radiotherapy* (IMRT), just an unnecessary object creating scattered radiation and contributing to increased amounts of leakage radiation (Vassiliev, *et al.*, 2006b).

In a study performed in 1991 by O'Brien *et al.* the flattening filter was removed to increase the output and reduce the treatment time for stereotactic radiosurgery with a 6 MV photon beam delivered by a Therac-6 linear accelerator (Atomic Energy of Canada Ltd., Mississauga, Ontario, Canada). For these treatments as much as 25 Gy is delivered in one session. With a flattening filter in the beam line, the beam-on time for one of these sessions was about 15 minutes. Removing the filter reduced the beam-on time to about 7 minutes. The field sizes used in these treatments are small (approx. $5 \times 5 \text{ cm}^2$) and within this field size they found a 5 % variation of dose rate. The out-of-field dose was also slightly reduced as a consequence of the removal of the scatter producing flattening filter (O'Brien, *et al.*, 1991).

It has been proposed by several authors that removal of the flattening filter from a conventional accelerator could be beneficial for IMRT treatments (Fu, *et al.*, 2004, Mesbahi, 2007, Mesbahi, *et al.*, 2007, Titt, *et al.*, 2006a, Titt, *et al.*, 2006b, Vassiliev, *et al.*, 2007a, Vassiliev, *et al.*, 2006a, Vassiliev, *et al.*, 2006b). For IMRT treatments, a uniform field is not a necessity as the treatment fields normally includes a variation of the photon energy fluence across the fields (Titt, *et al.*, 2006a). This variation of fluence can be shaped by the MLC leaves and in theory the flattening filter only decreases the beam output and adds a substantial amount of undesired scattered radiation to the patient (Fix, *et al.*, 2001). Pönisch, *et al.* (2006) found that the softer photon spectrum from a flattening filter free beam reduces the *multi leaves collimator* (MLC) leakage by about 20 %. This implies that the unflattened dose profile will not be an objection to shaping fields with the MLC.

The only commercially available medical linear accelerator without flattening filter is the Tomotherapy system (Hi-ARTII, TomoTherapy Inc., Madison, WI, USA). This system differs from conventional radiotherapy systems in that it is a dedicated IMRT unit and hence no flattening filter is needed in the beam line. Instead, an electron stopper and a beam hardener together with a compact primary collimator, a 64-leaf binary MLC and a secondary collimator are used to achieve the desired fields. The radiation fields from this system are fan shaped with a maximum size of $40 \times 5 \text{ cm}^2$ defined by the secondary collimator. The complete treatment is delivered to the patient in a helical way by simultaneous motion of the couch and the radiation source, which is mounted on a rotating gantry, thus resembling the set-up of a computed tomography x-ray scanner. The radiation characteristics from this machine includes increased beam intensity in the centre of the field by a factor of approximately two, reduced spectral variation across the field and, owing mainly to the increased shielding of the collimators, a lower out-of-field dose. Except for the latter effect, it is the removal of the flattening filter that provides for the enhancement of the beam characteristics and, to some extent, provides for an ideal situation for IMRT treatments (Jeraj, *et al.*, 2004).

Previous investigations of the properties of conventional accelerators without flattening filter have mainly been conducted on Varian accelerators (Varian Medical Systems, Palo Alto, CA, USA). Some of them have included a 2 mm thick copper plate in the beam line, positioned at the same place as where the flattening filter would have been, mainly in order to remove contaminating electrons originating from the target.

A summary of studies of the dosimetric properties of conventional accelerators where the flattening filter has been removed is presented in Table 1.1.

Table 1.1. Papers investigating dosimetric properties of conventional linacs operating without flattening filter. Some are based on measurements and some on Monte Carlo simulations with either BEAMnrc or MCNPX code.

Author	Accelerator	Filter in beam line	Data collection	Studied properties	Nominal energy with filter
Fu et al. (2003)	BJ-6B	-	Measurements	Treatment plans	6 MV
Vassiliev et al. (2006a)	Clinac 2100	-	BEAMnrc	Depth dose, profiles, dose rates, out-of-field dose, output factors, head scatter factors	6, 18 MV
Vassiliev et al. (2006b)	Clinac 21EX	2 mm Cu	Measurements	Depth dose, profiles, output factors, MLC transmission	6, 18 MV
Titt et al. (2006a)	Clinac 21EX	-	MCNPX	Depth dose, profiles, photon and electron fluence, output factors, out-of-field dose	6, 18 MV
Pearson et al. (2006)	Elekta SL25	-	BEAMnrc	Depth dose, profiles, photon fluence,	6, 10 MV
Pönisch et al. (2006)	Clinac 21EX	2 mm Cu	Measurements and MCNPX	Depth dose, profiles, output factors, MLC transmission	6, 18 MV
Titt et al. (2006b)	Clinac 2100	2 mm Cu 11 mm Nylon No filter	BEAMnrc and MCNPX	Backscatter to monitor chamber	6, 18 MV
Zhu et al. (2006)	Clinac 21EX	2 mm Cu	Measurements	Head scatter factors	6, 18 MV
Mesbahi et al. (2007)	Elekta SL25	-	MCNP4C	Depth dose, profiles, photon and electron spectra, output factors, out-of-field dose	6 MV
Mesbahi (2007)	Clinac 21EX	-	MCNP4C	Depth dose, profiles, photon spectra, absolute dose, out-of-field dose	6 MV

Many of the studies presented in Table 1.1 have shown that removal of the beam modifying filter from a conventional linac could increase the delivered dose rate by approximately a factor of two at the central axis (Fu, *et al.*, 2004, Mesbahi, 2007, Mesbahi, *et al.*, 2007, Pearson, *et al.*, 2006, Titt, *et al.*, 2006a, Vassiliev, *et al.*, 2006a, Vassiliev, *et al.*, 2006b).

Fu, *et al.* (2004) showed in a planning study that the beam-on time of IMRT treatments without flattening filter could be reduced by 43 %, because of the higher dose rate. They compared IMRT treatments delivered with a BJ-6B linear accelerator (Beijing Medical Equipment Institute, Beijing), equipped with Elekta, Siemens or Varian-type MLC, with and without a flattening filter in the beam line. The treatment plans were created in the Focus *treatment planning system* (TPS) version 3.2.1 (CMS Associates, St. Louis, MO, USA) using a *pencil beam* (PB) kernel convolution algorithm. It should be noted that the actual reduction in treatment time is much less since the beam-on time is relatively short when the complete treatment time is taken into consideration. However, this does not advocate the use of a flattening filter for IMRT treatments.

Definition of penumbral width of the radiation fields is a difficulty in flattening filter free beams. The traditional definition, i.e. the distance between the positions of, e.g. 80 % and 20 % of the dose at the central axis ($P_{80/20}$), might not be comparable between flattening filter free and flattened dose profiles. The reason for this is that at the field edge, the dose is lower than at the central axis, thus the 90 % and possibly the 80 % dose point, will be inside the field for larger field sizes. The same problem arises for the definition of dosimetric field size, normally defined as the distance between the 50 % dose points. Due to the in-field dose fall-off, this distance can be slightly shifted for flattening filter free beams.

One method to compensate for the problems mentioned above has been introduced by Pönisch, *et al.* (2006). Instead of normalising the unflattened beam profiles to the central-axis dose value, they used a normalisation dose, which accounts for the in-field dose variation. The normalisation factor for the flattening free beam profile, D_n , was taken as the ratio of dose at the inflection point of the penumbral region of the flattened profile, D_u , and the dose at the inflection point for the unflattened profile, D_f , multiplied by the dose value at the central axis of the flat profile:

$$D_n = \frac{D_u}{D_f} D_{CAX} \quad (1)$$

In Figure 1.2, an illustration of two profiles normalised according to the method described above with the definitions of penumbral width and the off-axis position of the 50 % dose point (x_{50}). The black numbers indicate the ordinate axis for the normalised dose and the red scale is the scale normalised to the central-axis value for the unflattened beam.

The normalisation method described above has also been implied by others (Mesbahi, 2007, Mesbahi, *et al.*, 2007). The reported results from the three studies using the normalisation method defined by eq. 1 (including Pönisch *et al.* (2006)) showed a slight reduction of the penumbral width for flattening filter free profiles compared to flattened. Both computer simulated and measured values of the $P_{80/20}$ for a photon beam by Pönisch, *et al.* (2006) resulted in an average reduction of 0.6 mm for the flattening free beam for a field size of 10×10 cm² using an incident electron beam energy producing a 6 MV photon beam with the flattening filter. Monte Carlo simulations by Mesbahi, (2007) showed, for the same accelerator (Varian Clinac 21EX) and energy, that the reduction of $P_{80/20}$ was 0.15, 0.8 and 1.2 mm for field sizes of 5×5 , 10×10 and 20×20 cm², respectively. For the same field sizes Mesbahi, *et al.* (2007) calculated, using the Monte Carlo method, penumbral reductions of 0.4, 0.5 and 0.38 mm respectively using the same beam energy as above delivered by an Elekta SL-25. These changes are small but consistent for all field sizes.

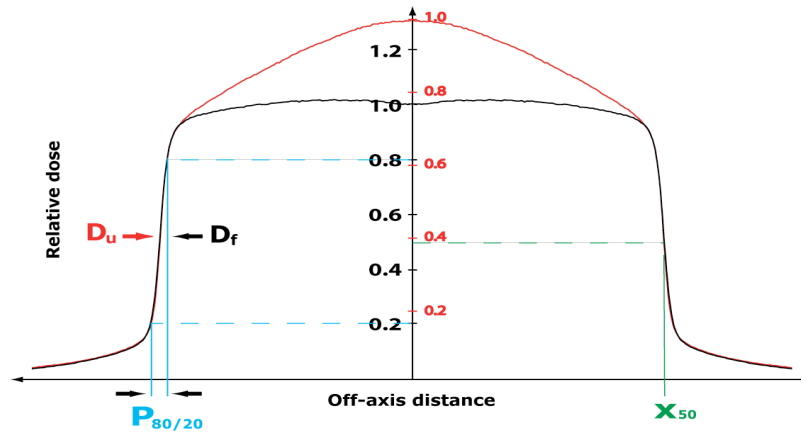


Figure 1.2 Illustration of two normalised profiles. The flattened profile (black) is normalised to the central-axis value and the unflattened profile (red) is normalised to the inflection points of the two profiles, D_u and D_f . The red numbers show the relative dose if normalised to the central-axis value of the unflattened profile. Also shown are the definitions of penumbral width and the point of 50 % of the normalised dose.

The dosimetric field edge was evaluated by calculating the distance from the central axis to the off-axis point where the dose was 50 % of the normalised dose, using the same method as described above. For a $10 \times 10 \text{ cm}^2$ field at a depth of 10 cm in water, the x_{50} point was 0.6-0.7 mm closer to the central axis when no flattening filter was present in the beam line (Mesbahi, 2007, Mesbahi, *et al.*, 2007).

A reduction of dose outside of the treatment field for flattening filter free beams is also reported in several studies, not only for Tomotherapy machines where an effective shielding and thick MLC leaves are the main contributors to a reduced leakage (Jeraj, *et al.*, 2004). When the flattening filter is removed from conventional linacs, one of the largest sources of scattered radiation from the accelerator is removed. This should, in combination with the increased dose rate at the central axis and subsequent reduction of MLC leakage, result in decreased out-of-field doses. Titt, *et al.* (2006a) found a significant reduction of the in-field-scatter photons at positions close to the treatment field. This is also in agreement with others (Mesbahi, 2007, Mesbahi, *et al.*, 2007, O'Brien, *et al.*, 1991, Vassiliev, *et al.*, 2006a, Vassiliev, *et al.*, 2006b), although some of the authors of these studies claimed the reduction to be too small for any practical advantages.

1.3.1 Portal Imaging

Portal imaging is the acquisition of images with a radiotherapy beam, mainly in order to confirm the patient setup. However, these images suffer from low contrast and sharpness because, for photons in the MeV range, the attenuation properties of bone and soft tissue are nearly identical since Compton scattering is the dominant interaction. The electronic cross-section for Compton-interactions is essentially independent of the atomic number, Z , and hence images will be sensitive only to differences in density and not in Z . The softer photon spectrum from an unflattened beam could be utilised for improved portal imaging properties (Tsechanski, *et al.*, 1998).

Tsechanski, *et al.* (1998) investigated portal images from a flattening filter free beam produced by a thin target. This approach enabled a large fraction of low energy photons to reach the treatment field and they found that images taken with this beam had a better spatial resolution and better contrast.

The improvement of images when the unflattened beam is used has mainly two reasons. The cross-section for Compton-scattering is increased because of the lower energy photons present and for lower energies, more of the Compton scattered photons are scattered by a larger angle and therefore it is less probable that these photons reach the imaging detector (Tsechanski, *et al.*, 1998).

1.3.2 Tumour Dose Enhancement with High Z-material

Another application, which could benefit from the softer photon spectrum from a flattening filter free beam, is the use of contrast media for dose enhancement in tumours. Monte Carlo simulations by Robar, *et al.* 2002, indicated that in tumours with an uptake of gadolinium or iodine contrast media the dose-enhancement effect would be twice as high if an unflattened and unfiltered beam was used instead of a 6 MV flattened one, using the same incident electron beam. One of the advantages in being able to deliver these treatments with a megavoltage beam instead of the conventional orthovoltage beam is the build-up effect present in the higher energy beam, sparing the skin and bone from high doses.

1.4 Treatment Planning System

The off-axis softening of the spectrum from a flattened beam will introduce some undesirable characteristics of the beam. For the TPS this effect will introduce errors in the calculations of beam transmission through beam modifiers, e.g. wedges, for which one generally assume that the beam has similar transmission properties over the entire field (Zefkili, *et al.*, 1994). When using asymmetric fields, i.e. fields not symmetric with reference to the central beam, the off-axis softening introduces significant errors in the calculation of the dose distribution (Lutz and Larsen, 1984). Some dose-calculation algorithms do consider the off-axis softening, e.g. *collapsed cone* (CC) algorithms in Helax-TMS and Oncentra MasterPlan (Nucletron B.V., Veenendaal, The Netherlands). However, most of the PB dose-calculation algorithms do not take the off-axis softening corrections into account, e.g. PB algorithms in Oncentra MasterPlan (Oncentra MasterPlan *Physics and Algorithms*). This indicates that removal of the beam-modifying filter could improve the accuracy of dose distributions calculated with these PB kernels.

Studies regarding IMRT treatment-plans delivered with unflattened beams show slight differences compared to plans delivered with beams where a flattening filter is present in the beam line. Vassiliev, *et al.* 2007a, compared IMRT-treatment plans for ten prostate cancer patients. They used 6 MV photon beams from a Varian Clinac with a flattening filter and flattening filter free beams with the same incident electron beam energy. The treatment plans were created using the TPS Eclipse 8.0 (Varian Medical Systems). They found that the dose distributions were similar, although the flattening filter free plans produced a slightly more uniform coverage of the *planning target volume* (PTV), better conformity and a lower rectal dose. In this study no re-calibration of the monitor units was performed when the flattening filter was removed, hence a reduced amount of monitor units required for a treatment would show an increased “efficiency” for this beam. They concluded that the major advantage of the flattening filter free beam is the increase in output, which led to a reduction of monitor units per treatment by a factor of two.

1.5 Radiation Safety

The neutron production has been found to be lower for the unflattened beam operating at 18 MV. The neutron dose from a complete IMRT treatment of prostate cancer with no filter present in the beam line was estimated to be 69 % of the dose from a conventional treatment. This corresponds to a reduction of the risk of fatal secondary malignancies from 2.9 to 0.9 % (Kry, *et al.*, 2007).

Vassiliev, *et al.* 2007b, have been comparing doses outside the treatment room for beams with and without flattening filter for flattened beam energies of both 6 and 18 MV using the same incident electron beam energy for the unflattened beams. Their results showed a reduction of primary and scattered photons from the flattening filter free beam. They also found that for high-energy beams (18 MV) the induced radioactivity in the treatment room was lower when the flattening filter was removed, with the consequence of a lower radiation exposure of the radiotherapy staff.

2 Material and Methods

2.1 The Accelerator

Measurements of the flattening filter free beam were performed at St. Luke's Hospital, Dublin, Ireland. The accelerator used in this study was an Elekta Precise (Elekta Oncology Systems, Stockholm, Sweden), used clinically to deliver a 6 MV photon beam and electron beams of various energies.

The accelerator is equipped with asymmetric collimation jaws and a MLC consisting of 40 leaves on each side, allowing a maximum field size of $40 \times 40 \text{ cm}^2$, for an illustration of the accelerator components, see Figure 1.1.

2.1.1 Filter Configuration

The accelerator was modified for the production of an unflattened beam profile using the same incident electron beam energy as in the 6 MV flattening filter x-ray mode. The modification consisted of replacing the cone-shaped flattening filter made of iron with an about half a cm thick plate of copper (Figure 2.1). The main reasons for using this filter were to remove excessive electrons that do not interact within the target, to harden the beam spectrum and to facilitate the delivery of a stable beam. Elekta Medical Systems administered the construction and design of the filter.



Figure 2.1 A conventional flattening filter for a 6 MV beam (left) and the copper plate used in the flattening filter free mode (right).

The copper disk was positioned in a free slot on the second filter carousel. This carousel has a total of five slots containing electron foils and flattening filters (Figure 2.2). For a specific irradiation mode the desired filter is rotated into the beam line by a stepping motor and two independent interlocks ensures that a correct rotation has taken place.

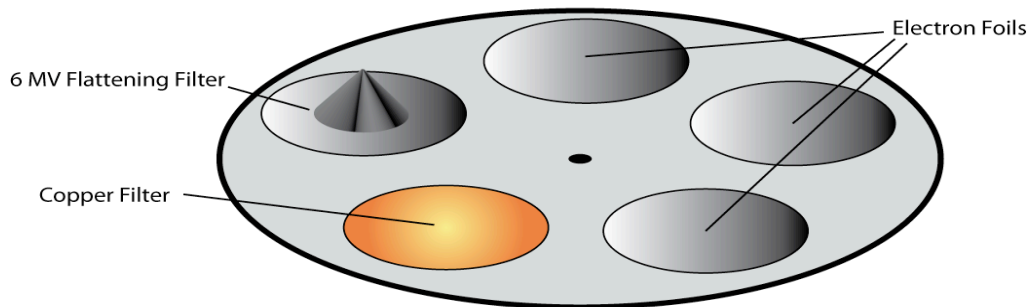


Figure 2.2 *The secondary filter carousel containing flattening filter, copper filter and electron foils. The carousel is situated below the primary collimators and the correct filter is rotated into the beam line for delivery of the desired beam.*

2.1.2 Beam Set-up

Without a flattening filter in the beam line, the machine settings, such as beam steering, dose rate, and many more, need to be configured. This was performed in collaboration with an Elekta engineer. The beam was adjusted until a symmetric field about the central axis was obtained, although the energy of the electron beam hitting the target remained unchanged. The gantry angle was kept at zero degrees and to ensure that the beam was parallel to the central axis, measurements were performed at various depths. For these measurements a PTW MP3 water phantom (PTW-Freiburg, Freiburg, Germany) was used together with a p-type diode (PTW, type 60008). To compensate for beam output variations, a cylindrical ion-chamber (PTW, type 31010) was used as a reference in the present and all of the following relative dose measurements.

To avoid the risk of delivering a flattening filter free beam when treating patients, the clinical hard drive was replaced with a research disk containing the calibration blocks that enables the unflattened beam to be delivered. When running the flattening filter free beam, the clinical disk was replaced with the research disk and the operation of the accelerator was managed in service mode. Measurements were only performed on the flattening filter free beam since measurements on the conventional beam already existed. The field size was not adjusted for the new beam so all reported field sizes are the nominal field sizes for the flattened beam. No wedged fields were investigated in this study as the unflattened beam is supposed to be used for IMRT treatments where wedges are obsolete.

2.2 Experimental Data Collection

Measurements of depth-dose curves, lateral dose profiles, output factors and beam quality were performed with the PTW-MP3 water phantom with inner tank dimensions of $694.0 \times 596.0 \times 502.5 \text{ mm}^3$ (Figure 2.3). The scanning system of this phantom consists of a slider and arms driven by stepper motors that allow for a position accuracy of $\pm 0.1 \text{ mm}$ and a reproducibility of the positioning of the probe of $\pm 0.1 \text{ mm}$. For all measurements with the water tank scanning system a PTW-MULTIDOS electrometer was used and the data collection was governed by the MEPHSTO version 6.0 (**Medical Physics Tool**) software from PTW.



Figure 2.3 *The Elekta Precise accelerator at St. Luke’s Hospital, Dublin and the PTW-MP3 water tank used for measurements of the flattening filter free beam.*

2.2.1 Central-axis Depth-dose

For measurements of the depth-dose dependencies, a cylindrical semiflex ion-chamber (PTW, type 21010), with an inner cavity volume of 0.125 cm^3 was mounted on the water tank scanning system. The chamber position was shifted 0.6 times the radius of the chamber towards the surface for correct positioning of the chamber reference point.

Measurements of the relative depth dose were carried out by starting the data collection from a water depth of 35 cm and, in steps of 1 mm, collecting values until the probe reached the surface. Depth-dose curves were measured at four different field sizes: 5×5 , 10×10 , 15×15 and $20 \times 20 \text{ cm}^2$ with a SSD of 90 cm. Since the stopping power variation with depth is relatively small, the depth-ionization curve was assumed to represent the depth-dose curve (Andreo and Brahme, 1986).

2.2.2 Profiles

For measurements of lateral dose profiles, as for depth-dose curves, the MP3 water tank was used. In order to obtain a higher spatial resolution of the measurements, the ionization level was measured with a p-type diode (PTW, type 60008). Dose profiles were collected at the following depths: 1.5, 5, 10 and 20 cm and at each depth for field sizes of 5×5 , 10×10 , 15×15 and $20 \times 20 \text{ cm}^2$. The SSD was kept at 90 cm and for each profile the step size in the lateral direction was 1 mm. Both in-plane and cross-plane profile data were collected, i.e. along the major axes perpendicular to the inner and outer collimations, respectively, and measurements were performed until 60 mm beyond the field edge.

2.2.2.1 Penumbra Width

For evaluation of the penumbral width and dosimetric field sizes, the normalisation method by Pönisch, *et al.* 2006, described in Section 1.3, was used for the flattening filter free profiles. The flattened profiles were normalised to the central-axis dose value. Calculations of penumbral widths were performed on measured dose profiles for field sizes of 10×10 and 20×20 cm². The penumbral width was defined as $P_{80/20}$ of central-axis dose for the flattened profile and for the flattening filter free beam for the profile normalised to D_n . Since the measurements were conducted with a spatial resolution of 1 mm, the points of 80 % and 20 % dose were found by linear interpolations.

2.2.2.2 Dose Profile Variation with Respect to Depth in Water

The shape of the dose profiles for flattened beams varies with depth due to the variation of attenuation properties across the field, i.e. beam energy degradation with off-axis distance. This variation can be correlated to the path length of the beam in the flattening filter (Yu, *et al.*, 1996). As a consequence, the profile shape will be different at different depths in for example water. However, since unflattened beams have flat copper plate in the beam line, it has been shown that the spectrum of flattening filter free beams varies less over the radiation field and therefore, the dose profile from these beams vary less with depth (Vassiliev, *et al.*, 2006a, Vassiliev, *et al.*, 2006b).

In order to quantify the variation of the profile shape with respect to depth, Vassiliev, *et al.* (2006a) introduced the following approach. All profiles were normalised to unity at the central axis and, because of the beam divergence, the width of the profiles were set to unity at the off-axis distance point where the dose was 50 % of the central-axis value (x_{50}) for the flattened beam. The integral of relative dose value for these profiles was calculated for an interval between the central axis and the x_{50} point. The area, $\Delta A_{d1.5,d20}$, representing the difference between profiles at depths of 1.5 and 20 cm and the area, $A_{d1.5}$, under the profile at a depth of 1.5 cm were calculated, as schematically depicted in Figure 2.4. The ratio $\Delta A_{d1.5,d20}/A_{d1.5}$ will provide a measure of the profile variation with depth.

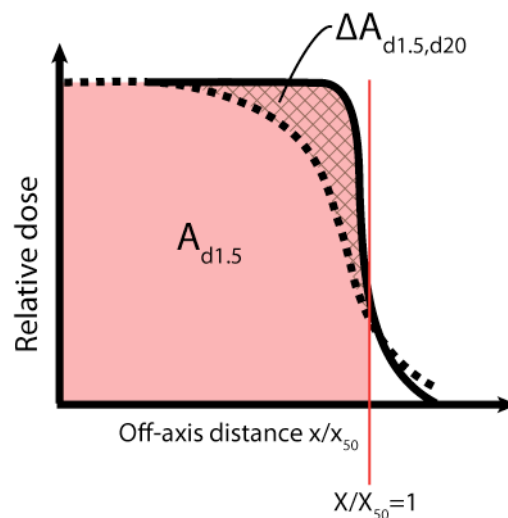


Figure 2.4 Illustration of $A_{d1.5}$ (red area) and $\Delta A_{d1.5,d20}/A_{d1.5}$ (grids). The dotted line represents the dose profile at a depth of 20 cm and the solid 1.5 cm. The red line marks the position of x_{50} for the flattened profile.

Calculations were performed on measured profiles with field sizes of 5×5 , 10×10 and 20×20 cm². The integration was performed as a summation of the dose values between the central axis and the position of x_{50} for the unflattened profile. The different number of measurement points for profiles at 1.5 and 20 cm depth was corrected for by scaling of the sum by the ratio of the number of values for the two profiles.

2.2.3 Output Factors in Air

The absorbed dose delivered by a linac is determined in a reference field under reference conditions. However, for non-reference collimation settings the dose output will differ from that of the reference. The main contributor to the change in output is the variation of the amount of secondary, scattered radiation, reaching the reference point (Zhu, *et al.*, 2006). To calculate the delivered dose in clinical treatments the variation in output for different field sizes must be evaluated. The output factor in air is normally defined as the variation of relative dose output for a specific field size relative to a reference field and the dose values are often measured at the isocenter, in accordance with IAEA TRS-398.

Measurements of the in-air output factors were performed using a water equivalent mini phantom, CIRS Model 670-S (Computerized Imaging Reference Systems Inc., Norfolk, VA, USA). This mini phantom has a cylindrical shape with a diameter of 40 mm and the reference point of the ion-chamber will be located at a depth of 10 cm in the phantom (Figure 2.5). The ion-chamber was a Farmer type ion-chamber (PTW, type 3010) with an active volume of 0.6 cm³. The phantom was positioned with the central axis of the beam coinciding with the central axis of the mini-phantom cylinder. The ionisation current was collected with a PTW-UNIDOS electrometer.

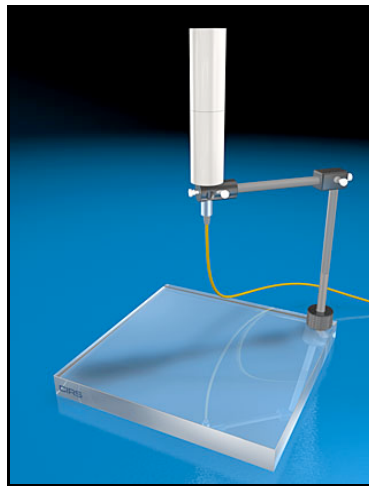


Figure 2.5 CIRS Model 670-S mini phantom consisting of Plastic Water[®].

In order to obtain correct measurements, the radiation field has to cover the whole diameter of the phantom, i.e. a minimum field size of 4×4 cm² is required for the mini phantom. Measurements were performed on symmetric fields with field sizes of 5×5 , 10×10 , 15×15 , 20×20 and 40×40 cm² and asymmetric fields where the outer or inner jaws were kept at a distance of 40 cm and the distance between other jaws was varied between 3, 5, 8, 10, 15, 20, 30 and 40 cm. For the 3×40 (outer \times inner) and 40×3 cm² fields, a cylindrical 0.125 cm³ semiflex ion-chamber covered with a brass build-up cap was used. This ensured that the whole of the detector, used for these small fields, was irradiated.

This ion-chamber was also positioned at the isocenter and in order to collect the output factor, measurements on the small fields were followed by reference measurements for the $10 \times 10 \text{ cm}^2$ field. For each measurement, 100 monitor units were delivered and, to obtain the head scatter factor, the ionization values for all measurements were normalised to the value of the $10 \times 10 \text{ cm}^2$ field.

2.2.4 Output Factors in Water

Output factors in water accounts for the variation of machine output in a water phantom. Just as for the output factor in air, different field sizes allow for a different amount of scattered radiation to the reference point. The output factor in water provides information about the variation of scattered radiation from the accelerator as well as the variation of scatter from the water phantom in a reference set-up.

Output factors for field sizes of 5×5 , 10×10 , 15×15 , 20×20 and $40 \times 40 \text{ cm}^2$ were measured with the same semiflex, 0.125 cm^3 ion-chamber and electrometer, used in previous water phantom measurements, and the values were normalised to the $10 \times 10 \text{ cm}^2$ field. The chamber was positioned at a depth of 10 cm in the MP3 water phantom with a SSD of 90 cm and 100 monitor units were delivered for each measurement.

2.2.5 Beam Quality

The beam quality measurements were performed according to *IAEA technical report series no. 398* where the beam quality is specified by the *tissue phantom ratio* TPR_{10}^{20} . The value of TPR_{10}^{20} can be determined by measuring the ionization or absorbed dose on the beam central axis at a constant *source chamber distance* (SCD) of 100 cm with a SSD of 90 cm and 80 cm for a field size of $10 \times 10 \text{ cm}^2$ (IAEA, 2000).

The beam quality measurements were conducted with a semiflex ion-chamber positioned at the isocenter in the water tank phantom. The SSD was varied from 90 to 80 cm by raising the water tank 10 cm while the ion-chamber was lowered by the same distance. The beam quality for a beam with flattening filter was obtained from measurements on a similar accelerator located at Lund University Hospital.

2.3 Monte Carlo Simulations

2.3.1 General Description of the Monte Carlo Simulation Technique

For the task of radiation transport calculation, analytical expressions are often inadequate. Because of the complex nature of radiation transport, these methods often require several simplifying assumptions, making them incapable of dealing with many of the problems that are of interest today (Rogers and Bielajew, 1990).

MC techniques are implemented for a wide variety of situations with a complex structure of probabilistic nature, e.g. radiation transport in matter. MC is used as a numerical technique to simulate the individual trajectory of each particle by using random numbers to sample from the statistical distribution of the physical processes involved. The probability distributions are derived from the underlying physical properties of the processes. Simulation of photons and electrons differ in some ways. When high-energy photons travel through a medium they undergo only a few interactions, since their mean free path is relatively large (in the order of decimetres in water). Each individual event can therefore be simulated according to the relevant probability distribution (Rogers and Bielajew, 1990).

A more complex situation occurs when simulating the transport of electrons and positrons through matter because of the large number of interactions they undergo as they slow down. As an electron slows down in a material it will be scattered elastically and inelastically hundreds of thousands of times, producing a large amount of low energy knock-on electrons (δ -rays) and leaving many atoms in excited states, until it is locally absorbed. To simulate each and every such event would be extremely time consuming (Rogers and Bielajew, 1990).

In order to handle the simulation of electrons, a condensed history technique was developed by Berger in 1963. In this technique a large number of individual electron interactions are grouped together into a single electron step. The energy loss and deflection occurring for every collision along this step is thus condensed into one event. The overall effect of these condensed histories is sampled from multiple scatter distributions determining the energy loss and deflection of the condensed step. The vast majority of the interactions an electron experiences results in minor changes in energy and direction and this is a requirement for the feasibility of the condensed history technique (Berger, 1963).

2.3.2 Accelerator Simulation with BEAMnrc

BEAMnrc (Rogers, *et al.*, 2005) is a Monte Carlo simulation code based on the EGSnrc (Electron Gamma Shower) radiation transport engine developed by Kawrakow in 2000. EGSnrc is an improved version of the EGS4 code (Nelson, *et al.*, 1985) and BEAMnrc is an improvement of the BEAM code (Rogers, *et al.*, 1995) implementing the EGSnrc code system. The development of the original BEAM code was part of the OMEGA project (Ottawa Madison Electron Gamma Algorithm). The purpose of that project was to develop a Monte Carlo technique capable of simulating a full 3-D electron beam treatment planning system. Extensive benchmarking of the BEAM code has been performed on a variety of accelerator models with good agreement with measurements of central-axis depth-dose curves and dose profiles. In BEAMnrc each primary and its secondary particles can be traced and thus, when a large number of particles are simulated, information about, e.g. the fraction of particles that interacted in a specific region, can be obtained (Rogers, *et al.*, 1995).

A particle history is started by creating particles with energy and coordinates stated by a source distribution defined by the user. All particles associated with the same primary particle are defined as one history.

In this study a model of a photon beam from an Elekta *Precise* accelerator, with and without a flattening filter, were simulated with BEAMnrc. The program allows for the construction of a user-specified accelerator head by defining its geometry through the use of a number of individual component modules (CMs). Component modules can be combined or modified to match the actual shape and composition of the real accelerator components.

The dimensions, materials and positions of the different accelerator components used in this study are based on the manufacturer's specifications. The accelerator model of the Elekta *Precise* accelerator used in this study consisted of the component modules presented in Figure 2.6.

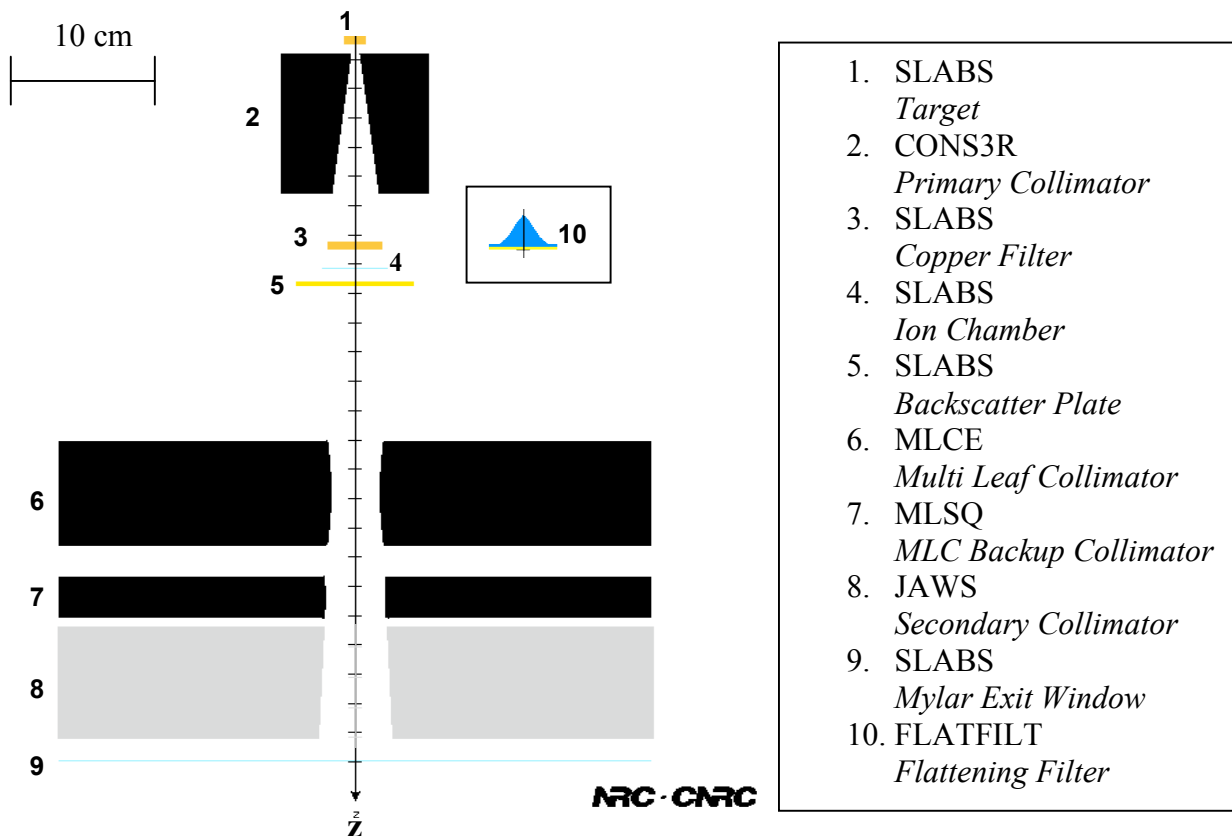


Figure 2.6 Schematic illustration of the accelerator head without flattening filter as it is seen in the xz-plane. The grey-coloured collimators would only appear in the yz-plane and have been added to the figure for completeness. The legend shows the different component modules and what they are used for.

Figure 2.6 is a cross section of the accelerator head in the xz-plane with the adding of the secondary collimators from the xy-plane. For simulations of the flattening filter free beam, the flattening filter was replaced with the copper plate. All simulations were modelled with the beam central axis following the z-axis.

The EGSnrc code uses what is called a class II procedure for simulation of electron interactions. As previously mentioned, a condensed history technique is used and energy losses along an electron step are grouped in such a manner that the energy is considered to be deposited evenly along this step, i.e. the electron step size is defined by the *stopping power value* according to the *continuous slowing down approximation (CSDA)*. In class II electron transport algorithms, the continuous slowing down is modelled by the *restricted stopping power*. The energy deposition along the electron step will be modelled by the restricted stopping power as long as the energies of bremsstrahlung photons and δ -rays are below the user defined threshold energy, AP and AE, respectively. All energy losses below the threshold will be deposited evenly along the electron step and energy losses above the threshold energy will be modelled separately (Rogers and Bielajew, 1990).

To estimate statistical uncertainties of the calculated results, BEAMnrc and DOSXYZnrc uses a history-by-history method implemented by Walters, *et al.* (2002). The uncertainty is calculated using the standard error formula:

$$s_{\bar{X}}^2 = \frac{1}{N-1} \left[\frac{\sum_{i=1}^N X_i^2}{N} - \left(\frac{\sum_{i=1}^N X_i}{N} \right)^2 \right] \quad (2)$$

where X_i is the quantity of interest scored in statistically independent history i , \bar{X} is the mean value of X and N is the number of independent histories, i.e. the number of initial particles.

2.3.3 PEGS4

The cross section data for the different materials used in an EGSnrc simulation is stored in a PEGS4 (Pre-processor for EGS4) file. This data can be created using the PEGS4 code in the EGSnrc program package. The user defines the lower bound for the production of knock-on electrons and photons by setting the values of, AE and AP, respectively. These values represent the lower limit of the cross sectional data in the PEGS4 file (Kawrakow and Rogers, 2002).

2.3.4 Variance Reduction Methods

MC simulations attempting to simulate the full stochastic development radiation transport through the simulated accelerator head can, if a low variance is requested, be very time consuming. The efficiency, ε , of a Monte Carlo calculation can be described by the equation

$$\varepsilon = \frac{1}{Ts^2} \quad (3)$$

where T is the central processing unit (CPU) time required for the calculation and s is the statistical uncertainty of the quantity of interest (Rogers and Bielajew, 1990). The computational time is directly proportional to the number of histories in a simulation, N , and the efficiency is thus proportional to the inverse of the CPU time required per particle history.

The uncertainty is related to N by:

$$s^2 \propto \frac{1}{N} \quad (4)$$

The idea behind the variance reduction methods described below is to provide means of reducing N , while s remains unchanged (or if one prefers, reduce T and s) when using the EGSnrc code system. This leads to the fact that when variance reduction methods are introduced, eq. 4 is no longer valid. It is of course required that these methods do not increase the computing time by, for example some detailed, expensive calculation performed for every particle step (Rogers and Bielajew, 1990). It is also important to note that some variance reduction techniques, e.g. transport cutoff and range rejection, can introduce systematic bias and therefore introduce systematic errors to the calculations (Verhaegen and Seuntjens, 2003). The transport cutoff and range rejection methods do in some way use approximations to achieve a higher computational efficiency, while the last of the methods described below, bremsstrahlung splitting, do not interfere with the physics while increasing the efficiency.

2.3.4.1 Transport Cutoff Energies

The most common technique for reduction of the calculation time in MC simulations is to introduce electron and photon cutoff energies, ECUT and PCUT, below which the particles are stopped and the remainder of their energy is deposited in the current region. The cutoff energies should be set in a way that will not affect the calculated result, i.e. the range of the particles should be as short, or shorter, as their distance to the boundaries of their current region. Since photons can travel relatively large distances, even low-energy photons in high- Z -material, the cutoff energy for photons must be smaller than for electrons. A rule of thumb is to set the electron cutoff energy so that the electrons' range at this energy is one third of the smallest dimension in the dose-scoring zone (Rogers, *et al.*, 2005).

2.3.4.2 Secondary Particles Production Thresholds

A variance reduction method previously discussed is the energy thresholds for production of secondary bremsstrahlung photons and δ -rays, AP and AE. Higher values of these thresholds will reduce the computational time required for the simulation. The production thresholds are required to be equal or lower than the particle transport thresholds, ECUT and PCUT. For dose calculations it is common to set AP=PCUT and AE=ECUT (Rogers, *et al.*, 2005).

2.3.4.3 Range Rejection

Range rejection of charged particles results in termination of the particles if their residual ranges are smaller than the distance to the nearest boundary or scoring region. This can save a great deal of computing time, since the range and distance to boundaries are already calculated by the EGSnrc code (Kawrakow and Rogers, 2002). The electron range is calculated as the pathlength travelled until it slows down to the cutoff energy, if the electron does not undergo any discrete interactions. The range is thus set conservatively since only a few electrons travel this far (Rogers, *et al.*, 1995).

As bremsstrahlung photons can be generated by the electron as it is slowing down, range rejection involves an approximation since these photons can escape the region and deposit their energy elsewhere. These effects can be minimised with the setting of a maximum energy, ESAVE, above which no range rejection is performed. This allows higher energy electrons to produce bremsstrahlung photons. The energy threshold has to be chosen depending on the simulation situation. For 10 MeV electrons incident on tungsten, about 7 % of the photon energy fluence is created by electrons with energies below 2 MeV.

With an energy threshold of 1 MeV for range rejection, the error will be 2 % or less in this situation (Rogers, *et al.*, 1995). It is important to turn off range rejection in regions where the bremsstrahlung process is an important interaction mechanism, e.g. in the target.

2.3.4.4 Bremsstrahlung Splitting and Russian Roulette

In order to increase the simulated bremsstrahlung production in the target and hence improve the statistics from these photons, BEAMnrc offers three different options of bremsstrahlung splitting: uniform, selective and directional. The simulations in this work were performed with the *selective bremsstrahlung splitting*, SBS, described below.

When a bremsstrahlung event occurs, the number of photons emitted is increased by a number, N_s , and each photon is given a weight equal to $1/N_s$ times the weight of the electron that generated them. The number N_s has a value somewhere between a maximum and a minimum value set by the user. In order to avoid tracking a large number of photons which will not make it to the scoring plane, N_s is dependent on the probability for the generated photons to reach the plane of interest. This probability is calculated using the incident electron energy and direction. If the photons have a high probability of reaching a user defined field of interest, N_s will be closer to the maximum value and if the direction and energy of the electron makes it unlikely for any photons created by it to reach the field of interest, N_s will be set to a lower value. A recommendation is to set the sides of the field of interest 10 cm larger than the largest side of the simulated treatment field (Rogers, *et al.*, 2005).

The energy and direction of each photon are sampled individually according to relevant probability distributions. The energy of the photon-generating electron is reduced by the energy of just one of the photons to preserve the effects of energy straggling. The consequence of this is that energy is not conserved for each history. Absolute conservation of energy would demand that the electron energy is decremented by the average energy of the photons. However, for a large number of splitting events, energy will, on average, be conserved (Rogers, *et al.*, 2005).

If the primary interest of the simulation is the bremsstrahlung photons, BEAMnrc can use what is called Russian Roulette on the secondary charged particles to reduce the CPU time required and to preserve the benefits of the bremsstrahlung splitting variance reduction. Russian Roulette is “played” by setting a survival threshold for the charge particle equal to the inverse of the splitting number, N_s . For each particle a random number is chosen and if this number is less than the survival threshold, the particle survives, and its weight is increased by a factor of N_s . If the random number is higher than this threshold the charged particles history is terminated. If a surviving charged particle undergoes a bremsstrahlung process, another photon splitting will occur in order to preserve the statistics of the original split photon. These higher-order bremsstrahlung photons and eventual annihilation photons will be split into a fixed number of photons set by the minimum value of N_s (Rogers, *et al.*, 2005).

2.3.5 Phase Space Files

MC simulations with BEAMnrc allows for creation of a phase space file in a scoring plane directly below a component module. A phase space is a data set containing information of position, direction, charge, multiple crossings, etc. for every particle that crosses the plane. These files can end up requiring substantial amount of disk space. Each particle crossing the plane requires 32 bytes of data, and to achieve low uncertainties several million particles are required in the phase space file (Rogers, *et al.*, 2005).

2.3.6 LATCH

A sophisticated option regarding the origin of particles is the LATCH variable. When building the accelerator model in BEAMnrc, the user has an option to associate a geometric region with one of 23 possible LATCH-bits. The LATCH settings in the simulations performed in this study were such that for every history, when a particle is created or interacts in any other way in a region, it will inherit the LATCH from that region. Different regions can be associated with the same bit, e.g. the all the CMs forming the collimators can be associated with the same bit even if it consists of several regions of different material (Rogers, *et al.*, 2005).

2.3.7 Phantom Simulation with DOSXYZnrc

To simulate energy deposition in a phantom the EGSnrc user code DOSXYZnrc, developed by the NRCC group, was used (Walters, *et al.*, 2005). DOSXYZnrc is a program used for absorbed dose calculations in three-dimensional phantoms. The phantoms are defined in a Cartesian coordinate system and the absorbed dose can be calculated in user specified voxels in the phantom. The phantom material can be set individually for each voxel or globally for the entire phantom. The uncertainty in the dose calculation is dependent on both the size of the voxels and of the number of histories in the simulation. The relationship between the number of histories required obtaining a desired statistical uncertainty in a voxel and the voxel size is given by the equation (Spezi, *et al.*, 2002):

$$s \propto \sqrt{\frac{1}{N} \frac{A_{beam}}{V_{voxel}}} \quad (5)$$

where N is the number of histories, A_{beam} , is the field size, V_{voxel} , is the voxel volume and s is the statistical uncertainty in one standard deviation (S.D.). For a given field size, in order to reduce the uncertainty by a factor of two, the number of histories needs to be increased by a factor of four or the voxel volume needs to be four times larger.

The inputs for the dose deposition calculations in this study are radiation fields created in BEAMnrc.

2.4 Data Calculations with the Monte Carlo Method

2.4.1 Parameter Settings

The particle transport parameters for all simulations were set as default except for Bremsstrahlung angular sampling where the full Koch and Motz distribution was used. It has been shown in previous studies that it is important to use the full equation for the simulations performed in this study (De Smedt, *et al.*, 2005, Vassiliev, *et al.*, 2006a). The electron cut-off energies for particle transport were set to $AE=ECUT=0.711$ MeV (kinetic and rest energy), and $AP=PCUT=0.01$ MeV based on recommendations in the literature (Rogers, *et al.*, 2005).

The variance reduction methods used were selective bremsstrahlung splitting with $N_{s_{max}}=500$ and $N_{s_{min}}=50$, Russian Roulette and range rejection was turned on and ESAVE was set to 1 MeV. It has been suggested to use a splitting factor between 200 and 1000 (Kawrakow *et al.*, 2004) and in this clinic it's been chosen to use 500.

2.4.2 Benchmark Calculations

One of the more difficult tasks in simulating the output from a medical linear accelerator is to find the appropriate initial electron beam properties. This beam has to produce a photon beam that matches the measured beam. Tuning of the input source must be carried out for every accelerator intended for simulation, since accelerators, even from the same vendor and of the same type, can have a slightly different output.

The two most important parameters of the primary electron beam are, according to most of the published data, the mean energy and radial intensity distribution, i.e. FWHM of the lateral spread (De Smedt, *et al.*, 2005, Sheikh-Bagheri and Rogers, 2002, Tzedakis, *et al.*, 2004). In this study it was investigated how these two parameters and the energy distribution, i.e. FWHM of the energy spread of the electron beam, affected the dose profiles and the depth-dose curves.

For conventional photon beams, depth-dose curves are sensitive to the mean energy of the incident electrons (De Smedt, *et al.*, 2005, Sheikh-Bagheri and Rogers, 2002, Tzedakis, *et al.*, 2004). Dose profiles have been found to be sensitive to both the radial intensity and the mean energy (De Smedt, *et al.*, 2005, Tzedakis, *et al.*, 2004). The simulation results were thus compared with corresponding measurements of depth-dose curves and lateral dose profiles.

For the flattening filter free beam, ten different combinations of electron beam parameters were simulated with BEAMnrc. All beams were parallel circular beams impinging normal to the target. The mean energies of the primary electrons were varied between 6.2 MeV and 6.5 MeV in steps of 0.1 MeV. This energy interval was chosen since the electron beam energy of a previously tuned accelerator of the same type with a flattening filter was within this interval. Two different, Gaussian shaped energy distributions with a FWHM of 0.5 and 1 MeV were used for each of the mean energies. In all but two simulations the radial distribution was also set to be Gaussian in shape with an FWHM of 1.1 mm and for two simulations it was set to 4 mm (Table 2.1). These two widths have been used in previous simulations of a FF beam from the same accelerator at the clinic.

The photon fields generated in BEAMnrc were 20×20 cm² large and they were used by DOSXYZnrc to calculate central-axis depth-doses and lateral dose profiles in a homogenous water phantom. The dimensions of the phantom were $40 \times 40 \times 40$ cm³ and it was positioned at a SSD of 90 cm.

Lateral dose profiles were calculated along the major axis parallel to the inner collimators, i.e. the x-axis, at a depth of 10 cm with a voxel size of $0.5 \times 1.0 \times 0.5 \text{ cm}^3$ (x, y, z) except at the central axis where the voxel was $1.0 \times 1.0 \times 0.5 \text{ cm}^3$.

Table 2.1. Simulated incident electron beam parameters used for the production of photon beams.

Mean electron energy [MeV]	FWHM of energy distribution [MeV]	FWHM of radial intensity distribution [mm]
6.2	0.5	1.1
6.2	1	1.1
6.3	0.5	1.1
6.3	1	1.1
6.4	0.5	1.1
6.4	1	1.1
6.4	0.5	4
6.4	1	4
6.5	0.5	1.1
6.5	1	1.1

Central-axis depth-doses were calculated in $1.0 \times 1.0 \times 0.25 \text{ cm}^3$ voxels along the central axis, except at a depth of 10 cm where a $1.0 \times 1.0 \times 0.5 \text{ cm}^3$ voxel size was used. This larger voxel size was chosen in order to allow for simultaneous lateral dose profile calculations and to reduce the uncertainties at this depth, although the spatial resolution was lowered. The calculated lateral dose-profiles were normalised to the mean dose value of voxels between -25 and 25 mm. In Figure 2.7, a schematic illustration of the geometry of the phantom is shown.

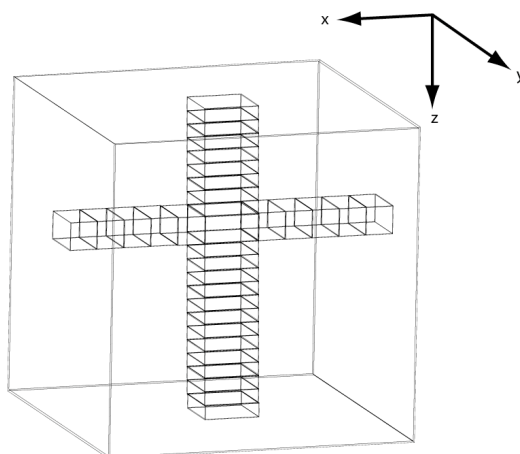


Figure 2.7 Voxel phantom used in calculations of depth-dose curves and lateral dose profiles. The voxel size was smaller in the z-direction except at the depth where the dose profile is scored (not to scale).

For every simulation, $1.5 \cdot 10^9$ histories were run in order to keep the dose uncertainties below 1 % in voxels inside of the radiation field and beyond the depth of maximum dose.

For the comparison between measured and calculated values, local dose differences were calculated for each initial electron beam. The local dose difference is defined as the difference between calculated and measured values of the dose in a single point divided by the measured value. The mean of this difference was also calculated for the complete profiles, the central ± 8.75 cm of the profiles and for the depth doses for depths beyond the depth of maximum dose.

2.4.3 Calculation of Lateral Dose Profiles and Depth-dose Curves

Lateral dose profiles and depth-dose curves were calculated with DOSXYZnrc in a similar way as for the benchmark calculations. Dose profiles were calculated at four different depths: 1.5, 5, 10 and 20 cm for both in-plane and cross-plane profiles with a field size of 20×20 cm². The voxel size was 0.5 cm in the direction of the calculated profile, 1 cm in other direction in the plane perpendicular to the beam axis and 2 cm in the direction parallel to the beam axis, except for the profile at 1.5 cm depth where the voxels was 0.5 cm in this direction. The number of histories was set to $2 \cdot 10^9$.

Depth-dose curves were calculated along the central axis for a 20×20 cm² field. The voxels were 0.25 cm in the direction of the beam line and 1 cm in the other two orthogonal directions. For these calculations $4 \cdot 10^9$ histories were simulated.

2.4.4 Phase Space Analysis

Information such as the distribution of particle energy, fluence, energy fluence and mean energy can be extracted from the generated phase space files using the utility program BEAMDP (BEAM Data Processor), included in the BEAMnrc program package. Another option is to use the so-called ZLAST information provided with each particle. ZLAST contain information about where along the z-axis a particle in the phase space file, photon or charged particle, last interacted. In BEAMDP the user can choose if information about photons, electrons, positrons, charged particles or all particles is requested. BEAMDP can also extract particles with specific LATCH-bits, and information about the fraction of particles interacting in certain regions can be obtained (Ma and Rogers, 1998).

For the analysis of phase space information six different beams were generated with two different field sizes: 10×10 and 40×40 cm², with and without a flattening filter in the beam line. For the smaller field size a water phantom was added at a SSD of 100 cm. The side of the square phantom was 50 cm and the depth was 20 cm and phase spaces were scored at a depth of 10 cm. For the 40×40 cm² fields a phase space file was generated in air at a SSD of 100 cm and at the downstream surface of the flattening filter. All phase spaces were scored in planes normal to the central axis.

2.4.4.1 Investigated Beam Properties

For the evaluation of photon fluence distribution in energy, the photon spectra were averaged in two different circles around the central axis. For the 10×10 cm² field a circle with a radius of 1 cm centered at the central axis and an annulus with an inner radius of 4 cm and an outer radius of 5 cm was used. When analysing the larger fields, the outer annulus was moved out towards the field edge having an inner radius of 17 cm and an outer radius of 18 cm.

Photon fluence, photon energy fluence and photon mean energy variations across the fields were extracted in annuli of equal area, with the centre of each circle at the central axis for the 10×10 cm² field. The mean energy of the primary photons across the field and the fluence of photons, which were created or had interacted in the flattening or the copper filter, were also investigated.

The off-axis variations of fluence etc., were, for the 40×40 cm² field, evaluated in rectangular bins centred on the major axis parallel to the MLC. The width of the rectangles was 2 cm and they were 0.5 cm in the direction of interest, i.e. parallel to the MLC.

The same phase space was used for analysing the angular distribution of photons in the entire field and the ZLAST option was used to extract the fraction of particles created in different areas of the accelerator head.

2.4.4.2 Half-value Layer Calculations

To further investigate the off-axis softening, calculations of the *half-value layer* (HVL) of water were carried out. As the radiation beam becomes softer with increasing off-axis distance when a flattening filter is present in the beam line, the HVL is decreasing (Zefkili, *et al.*, 1994). However, for the unflattened beam, primary photons, both at the central axis and off-axis, will pass through approximately the same amount of filter material. This implies that any spectral changes will depend on the angular distribution of the photons created in the target by the bremsstrahlung process. The energy distribution of the photons is close to the same over the entire field and the HVL should therefore remain constant across the radiation field. To outline the HVL variation with off-axis distance for a flattening filter free beam is of interest, since some dosimetry models, among them MasterPlan CC, base their correction for the off-axis softening on measurements of HVL, presented in Taylor *et al.* (1998) (Oncentra MasterPlan *Physics and Algorithms*).

Measurements of the variation of HVL as a function of the off-axis ray angle for several different medical linear accelerators are summarized in Taylor, *et al.* (1998). They have extracted a fit of this data that is used in, e.g. MasterPlan CC:

$$HVL/HVL(\theta) = 1 + 0.00181\theta + 0.00202\theta^2 + 0.0000942\theta^3 \quad (6)$$

where $HVL(\theta)$ represent measures at an angle θ and HVL represent the zero degree measure.

2.4.4.2.1 Evaluation of Phase Space for HVL

For the calculation of HVL at different off-axis distances, a phase space generated at 100 cm from the target with a field size of 40×40 cm² was used. In this plane 13 annular regions were defined with the central region having a radius of 1 cm and the outer regions forming annuli with a width of 1 cm. The off-axis distance of each annulus was set so that the photon rays entering the centre of it had an angle, θ , to the central axis, of one to twelve degrees in steps of one degree (Figure 2.8).

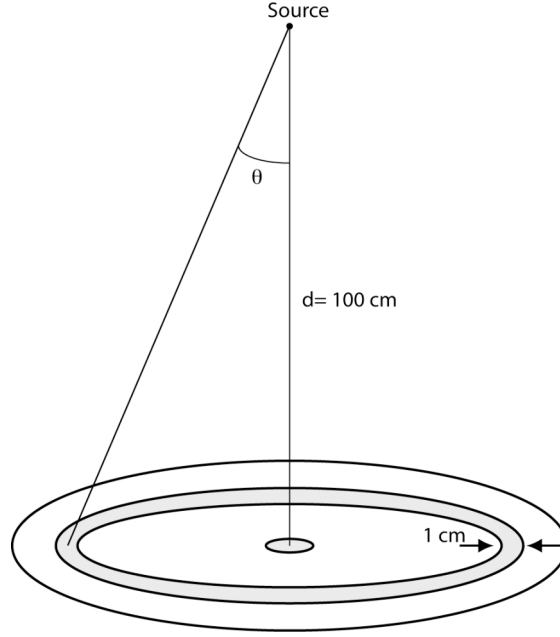


Figure 2.8 Illustration of the set-up for HVL measurements. Spectral information was extracted in annuli at an angle θ from the central axis. Each annulus has a width of 1 cm.

For the extraction of the necessary spectral information from the phase space files, the utility program BEAMDP was used. In order to simulate narrow beam geometry, photons interacting in other component modules than the target were excluded, using the LATCH variable. This ensured that no scattered photons would interfere with the measurements and narrow beam geometry was achieved.

For each of the angular regions described above, spectral information was extracted. The maximum energy of the photons in the phase space file was 7 MeV and the photon fluencies were calculated in 200 equidistance energy bins between zero and the maximum energy.

In this study, the half-value layer is defined as the thickness, t , of the material needed to attenuate the in-air collision kerma, K_c , (**k**inetic **e**nergy **r**elased in **m**atter) to half of its measure when no absorber was present. In order to calculate this thickness the following simple relation was used (Knöös, *et al.*, 2007):

$$K_c(t)/K_c(0) = \frac{\sum_{n=i}^N \varphi_i E_i \left\{ \frac{\mu_{en}(E_i)}{\rho} \right\}_{air} \cdot \exp[-\mu(E_i)_{absorber} \cdot t] \Delta E_i}{\sum_{n=i}^N \varphi_i E_i \left\{ \frac{\mu_{en}(E_i)}{\rho} \right\}_{air} \cdot \Delta E_i} = \frac{1}{2} \quad (7)$$

The summation was performed over N energy bins with energy fluence φ_i , mid-energy E_i , and energy width ΔE_i . The linear attenuation coefficient, μ , and the energy mass-attenuation coefficient, μ_{en}/ρ , for each energy bin were from the XAAMDI database (X-ray Attenuation and Absorption for Materials of Dosimetric Interest) (Hubbell and Seltzer, 1995).

Equation 7 was then applied to each of the 13 spectra extracted by BEAMDP and the value of $HVL/HVL(\theta)$ for each angle could be calculated.

3 Results and Discussion

3.1 Measurements

3.1.1 Lateral Dose Profiles

Lateral dose profiles measured without the flattening filter for different field sizes are presented in Figure 3.1. The SSD was 90 cm and the profiles were measured at a depth of 10 cm in water. All profiles are normalised to the central-axis dose values and they are shaped by the upper jaws, i.e. the MLC and back-up jaws. As clearly seen in the figure, the in-field dose variation is increased with field size. For the smallest field the dose profile is relatively flat within the field, the difference in relative dose between profiles with and without flattening filter is only about 2 % at an off-axis distance of 2 cm for the $5 \times 5 \text{ cm}^2$ field. For the $20 \times 20 \text{ cm}^2$ field the 95 % iso-dose is within a circular area of approximately 6 cm in diameter. This is comparable with reported measurements from O'Brien *et al.* (1991) where the 95 % iso-ionization level was within a diameter of 5 cm for a $40 \times 40 \text{ cm}^2$ field measured at a depth of 1.5 cm with SSD 100 cm.

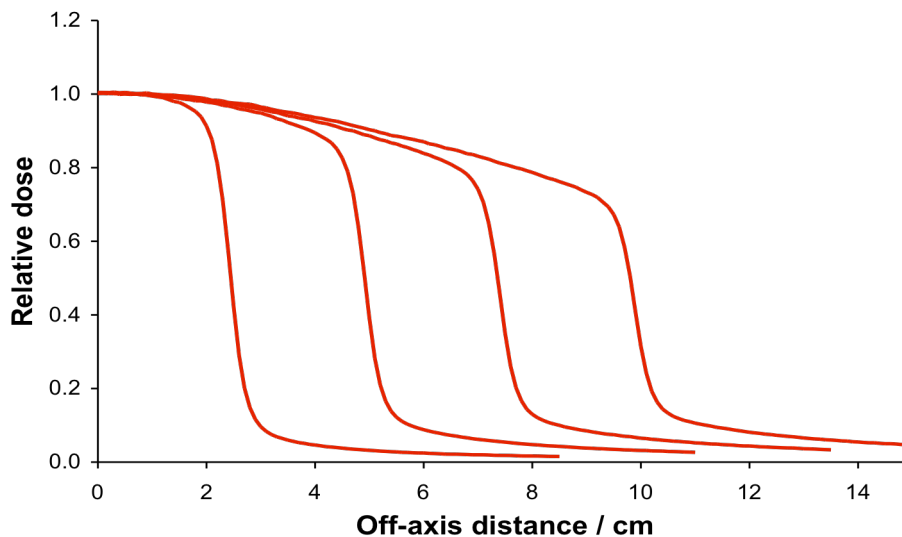


Figure 3.1 Measured profiles with the flattening filter free beam at a depth of 10 cm with a SSD of 90 cm. The field sizes are 5×5 , 10×10 , 15×15 and $20 \times 20 \text{ cm}^2$ and all profiles are normalised to the central-axis dose value.

3.1.1.1 Dose Profile Variation with Respect to Depth in Water

In Figure 3.2, measured profiles at four depths: 1.5, 5, 10 and 20 cm are shown for beams with (FF) and without (FFF) a flattening filter in the beam line. All dose profiles are normalised to the central-axis dose value and the off-axis distance is normalised to the position where the dose is 50 % of the central-axis value for the flattened profiles at each depth.

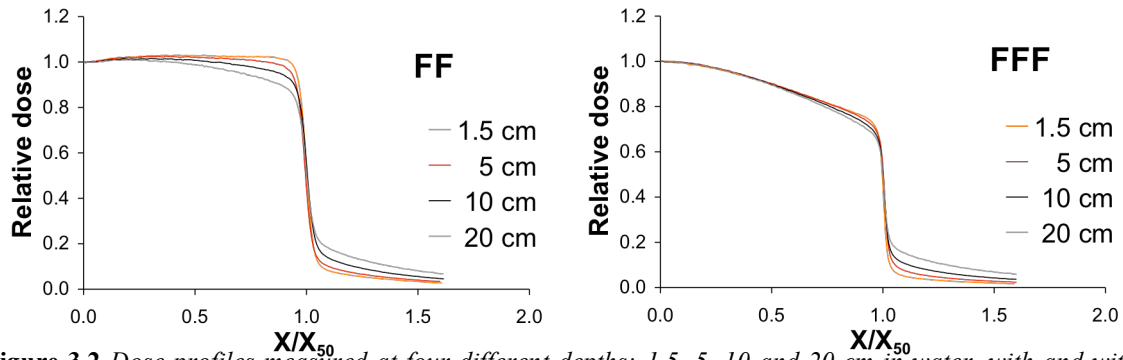


Figure 3.2 Dose profiles measured at four different depths: 1.5, 5, 10 and 20 cm in water, with and without a flattening filter in the beam line. The SSD was 90 cm and the dose values are normalised to the dose value at the central axis and the off-axis distances are normalised to the x_{50} -position for each profile.

In Figure 3.3, the variation of lateral dose profiles with depth is shown. The profiles are measured at two different depths: 1.5 and 20 cm, with and without a flattening filter in the beam line. The field size is $20 \times 20 \text{ cm}^2$ and the off-axis distance is normalised to unity at the position of 50 % dose for the flattened dose profiles.

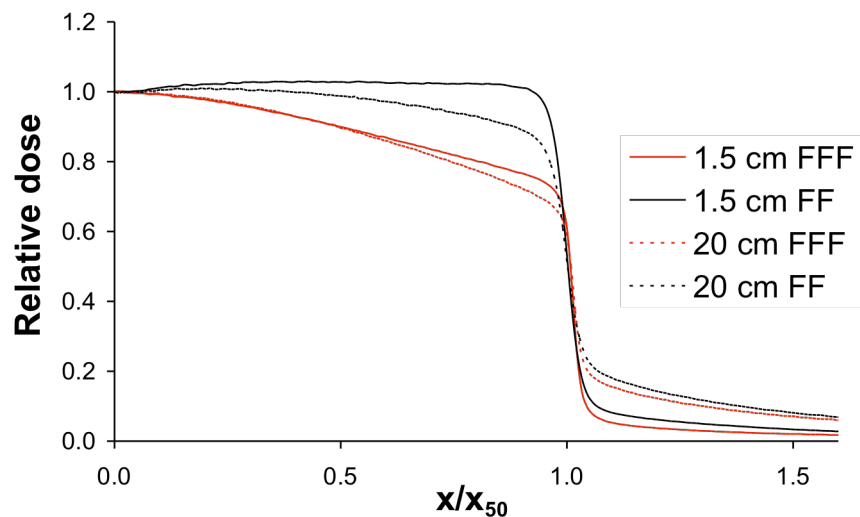


Figure 3.3 Measured profiles at two different depths: 1.5 (solid lines) and 20 cm (dotted lines,) for a field size of $20 \times 20 \text{ cm}^2$. The dose profiles without a flattening filter (red) and with a filter (black) are normalised to the dose value at the central axis. The off-axis distance is normalised to the x_{50} point for the flattened dose profile.

It is quite clear that the flattening filter free profiles varies less with depth, and to quantify the variation the ratio $\Delta A_{d1.5,d20}/A_{d1.5}$ (Figure 2.4) was calculated for two different field sizes: 10×10 and $20 \times 20 \text{ cm}^2$ (Table 3.1). The primary reason for the larger variation of profiles with the flattening filter in the beam line is the difference in beam quality across the field. The softer spectra at the field edges will result in more photon attenuation with depth than the harder photon spectra at the central axis and thus, when passing through water, the profile will be more and more cone-shaped. However, for flattening filter free beams, there is a constant amount of beam filtration across the field and the shape of the profiles varies less with depth.

For comparison, data from Vassiliev, *et al.* (2006b) is included in Table 3.1. Because these data were collected using a Varian Clinac 21EX with a 2 mm thick plate of copper in the beam line of flattening filter free beam and in the present study an Elekta Precise with an about half a centimetre thick copper plate was used, the two data sets are not entirely comparable. The differences between the two radiation modes are larger in this study. This might be explained by the harder beam spectrum for the flattening filter free beam used in this study compared to the beam used by Vassiliev, *et al.* (2006b).

A reduced variation of the profile shape at different depths can help improving the TPS dose-deposition calculations. The PB algorithm, in for example Oncentra MasterPlan, does not directly correct for the different photon beam hardening effect at off-axis positions, but uses a spatially invariant polyenergetic pencil beam, derived from central-axis depth-dose curves. For larger fields this results in an underestimation of the calculated dose deposition at the central axis, but also a too low dose at off-axis positions. With the flattening filter free beam, the impact of the spectral composition of the PB algorithm should be reduced because of the similar spectral composition in the entire treatment field.

Table 3.1 *The ratio $\Delta A_{d1.5,d20}/A_{d1.5}$, described in Section 2.2.2.1, in percent, for field sizes of 10x10 and 20x20 cm² with (FF) and without (FFF) a flattening filter. This ratio is a measure of the variation of dose profile shape at different depths. For comparison, the results of Vassiliev, *et al.* (2006b) for a Clinac 21X with a 2 mm copper plate in the beam line in FFF mode, are added to the table.*

This study		
Filter configuration	10x10 cm²	20x20 cm²
FFF	0.42	1.23
FF	2.70	4.82
Vassiliev, <i>et al.</i> (2006b)		
	10x10 cm²	20x20 cm²
FFF	2.0	2.0
FF	2.9	4.8

3.1.1.2 Penumbra Width

The average reduction of penumbral width, for both in-plane and cross-plane profiles, for the flattening filter free beam was found to be 0.6 mm for the $10 \times 10 \text{ cm}^2$ field and 0.075 mm for the $20 \times 20 \text{ cm}^2$ field. The reduction for the $10 \times 10 \text{ cm}^2$ field is the same as reported by Pönisch, *et al.* (2006) for a Varian Clinac 21EX with a 2 mm thick copper plate in the beam line. However, they did not find any difference in the reduction of the penumbra between MLC-shaped and jaw-shaped profiles, although the penumbral width, for both beam modes, are larger for the profiles shaped by the MLC due to the rounded edges of the leaves. In this study we found no penumbral reduction in the jaw-shaped profiles, but rather large reductions for the MLC-shaped ones. This might be due to the different design of the accelerators: the jaws are set outside the edge of the MLC for MLC-shaped fields and the MLC is totally withdrawn for jaw-shaped fields when using the Varian machine. This is off-course affecting the results.

For radiation fields passing close to organ at risk, the smaller penumbral width may lead to sparing of these organs. However, the dose sparing is probably quite small since the difference in penumbral width is small between the two irradiation modes.

The probable reasons for the reduced penumbral width are the reduced amount of scatter from the accelerator head and maybe also the softer photon spectra. The latter could affect the penumbra by giving rise to a larger attenuation in the rounded edge of the MLC and thus reduce the width of the penumbral region.

The uncertainties in the results presented are rather large and more accurate measurements and/or Monte Carlo simulations are required to confirm the reduction of penumbral width and its approximate size.

3.1.2 Depth-dose Curves

Measured central-axis depth-dose curves for photon beams with and without a flattening filter in the beam line are presented in Figure 3.4. The curves were measured with a field size of $20 \times 20 \text{ cm}^2$ and the data are normalised to the dose value at the depth of maximum dose. The values have been corrected from a SSD of 90 cm to a SSD of 100 cm with the assumption of an unchanged scatter factor. The softer spectra of the flattening filter free beam leads to a steeper drop in dose deposition beyond the depth of maximum dose. For comparison data for a 5 MV beam from BRJ Supplement 25 (1996) are included.

To quantify the properties of the different beams two parameters, fractional dose at a depth of 10 cm, D_{10} , and the depth where the fractional dose is 80 %, d_{80} , are reported in Table 3.2. The reported values for the 6 MV flattened beam and the unflattened beam are measured with a SSD of 90 cm. These values are corrected for a SSD of 100 cm with the assumption of an unchanged phantom scatter factor for the different SSDs. It can be seen, that the depth-dose dependency for the flattening filter free beam is comparable to the 5 MV beam with flattening filter. This suggests that one way of tuning the flattening filter free beam to match the depth-dose curves of the flattened beam would be to increase the energy of the incident electron beam energy of unflattened beam to somewhere around what should be used for a 7 MV flattened beam.

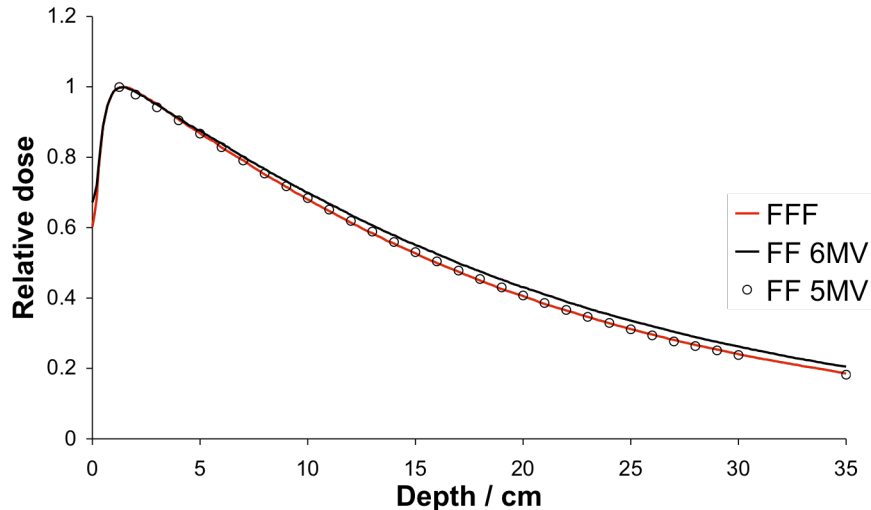


Figure 3.4 Measured depth-dose curves for a field size of $20 \times 20 \text{ cm}^2$ and for a SSD of 100 cm. The circles are values for a 5 MV beam from BRJ Supplement 25 (1996). The red line represents measurements on the flattening filter free beam performed in this work, the black line is for a beam with flattening filter and it is based on previous measurements. Both of these measurements are corrected from SSD 90 cm to SSD 100 cm.

Table 3.2 The fraction of maximum dose at a water depth of 10 cm, D_{10} , and d_{80} , the depth where the dose is 80 % of the maximum dose, evaluated from depth-dose measurements. The measured values for the 6 MV flattened beam and the unflattened beam are taken at the central axis with a SSD of 90 cm and are corrected for SSD 100 cm. For comparison, data for a 5 MV flattened beam from BRJ Supplement 25 (1996) are added.

	10×10			20×20		
	6 MV FF	FFF	5 MV FF	6 MV FF	FFF	5 MV FF
D_{10}	0.671	0.655	0.650	0.718	0.680	0.684
d_{80}	6.74	6.33	6.20	7.20	6.77	6.76

3.1.3 Output Factors in Air

Measurements of the output factor in air for square fields are presented in Figure 3.5. Since the variation in output for fields $>3 \times 3 \text{ cm}^2$ is caused by the different amount of scatter reaching the measurement point (Zhu and Bjärngård, 1994), removal of material in the beam line will reduce the variation of output for different field sizes. However, the copper plate in the beam line of the flattening filter free beam investigated in this study does also produce scattered radiation. The in-air output factor for this beam is therefore somewhere between the factor for the flattened beam and the beam without any beam-hardening filter from Zhu and Bjärngård, (1994) measured on a 6 MV beam from a Philips SL 75-5 accelerator (Figure 3.5). The scatter contributions from the two unflattened beams are almost constant between 20×20 and $40 \times 40 \text{ cm}^2$ and additional measurements on field sizes in between these might explain the reason for this behaviour. The reduced amount of material in the beam line is probably the main reason. For the flattened beams, the output factor varies between 0.973 and 1.033 for field sizes of 3×3 and $40 \times 40 \text{ cm}^2$, respectively. For unflattened beams with the copper plate, the corresponding variation is between 0.984 and 1.019.

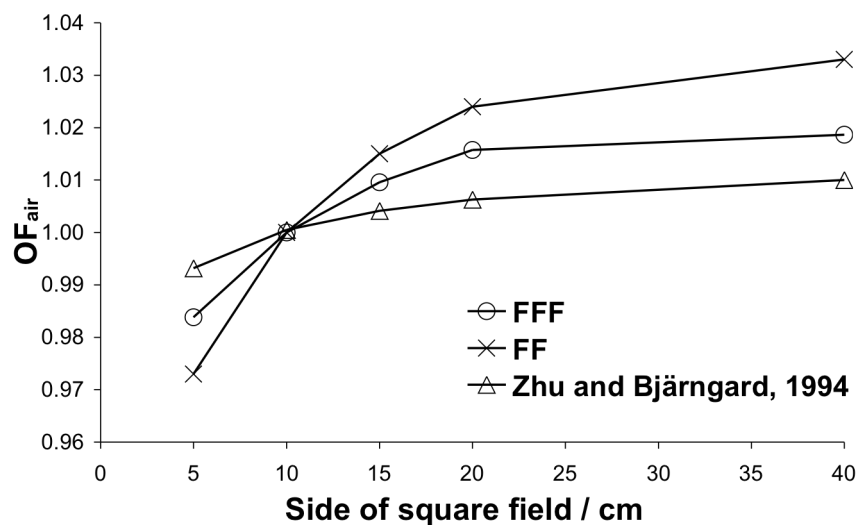


Figure 3.5 Output factor in air for square fields with field sizes of 5x5, 10x10, 15x15, 20x20 and 40x40 cm², measured with a mini phantom with the reference point located at isocenter (SCD=100 cm). Data for flattening filter free beams (circles) and flattened beams (crosses) are included as well as data from Zhu and Bjärngard (1994) where no hardening filter was present in the beam line (triangles).

Because of the different distance between the measurement point and the outer and inner jaws, the scatter from asymmetric fields will be depending on the jaw-setup. For some accelerators the positioning of the jaws will also affect the amount of backscattered radiation reaching the monitor chamber. However, the Elekta Precise accelerator is equipped with a backscatter plate reducing the impact of the difference in backscatter from the outer and inner jaws. In Figure 3.6 and Figure 3.7, output factors for rectangular fields with the outer, respectively inner collimators, set to generate a field width of 40 cm, while the other jaws are varied, creating a field width between 3 and 40 cm, are presented.

The inner jaws are positioned further away from the measurement point and thus, for the same field size, if the inner jaws are kept close together less scatter will reach the point of measurement than if the outer jaws are kept close. One of the reasons for this is purely geometrical; the measurement point “sees” less scattered radiation with the upper jaws. The effect is visible both for the flattened and unflattened beams. However, the effect is much less pronounced for the flattening filter free beam because of the lesser amount of scatter in this beam.

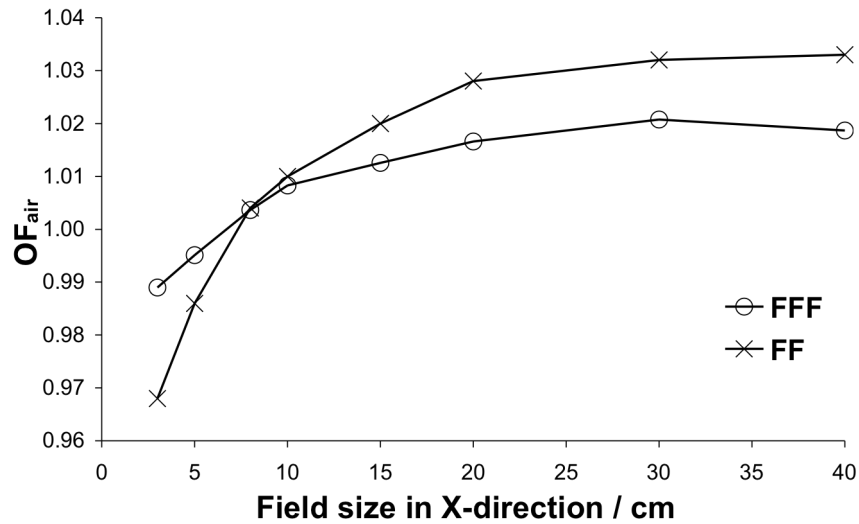


Figure 3.6 Output factors in air for different field sizes measured with a mini phantom with a SSD of 90 and the reference point of the chamber at a SCD of 100 cm. The field size in the y-direction, defined by the outer jaws is 40 cm and the inner jaws are varied creating a field width of 5, 8, 10, 15, 20, 30 and 40 cm. The smallest field was measured with an ion-chamber with brass build-up cap positioned at a SCD of 100 cm.

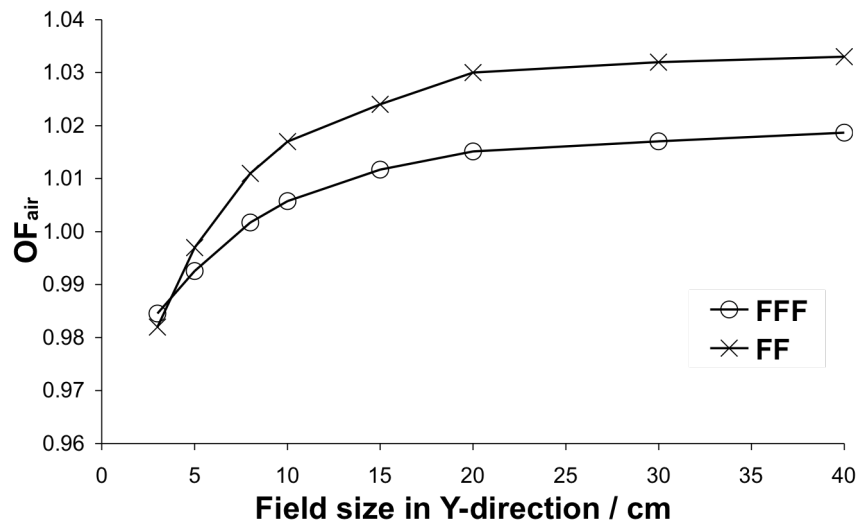


Figure 3.7 Output factors in air measured with a field size of 40 cm in the x-direction, defined by the inner jaws. The setup is the same as for Figure 3.6.

3.1.4 Output Factors in Water

The output factors in water show a similar difference between flattened and unflattened beams as for the output factors in air. The relative difference is however larger for the output factors, i.e. there is a decreased amount of phantom scatter when a flattening filter free beam is used. For the flattened beam the output factor in water is varied between 0.904 and 1.097 while for the flattening filter free beam this variation is between 0.915 and 1.076.

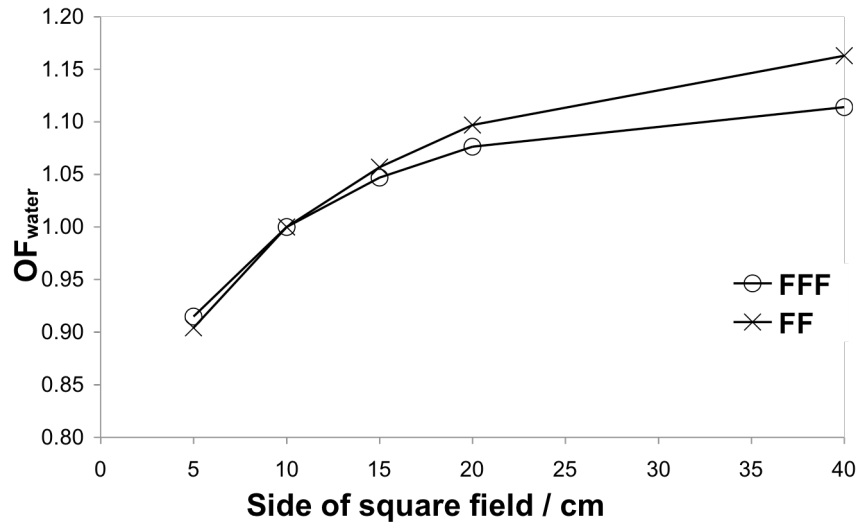


Figure 3.8 Output factors in water for square fields: 5x5, 10x10, 15x15, 20x20 and 40x40 cm² large. The output factors were measured at the isocenter (SCD=100 cm) and at 10 cm depth in water.

The reduced variation of output, both in air and in water, for the flattening filter free beam is a useful property, which may reduce the uncertainties in scatter corrections, implemented by treatment planning systems. For dose calculations of smaller fields, e.g. using the pencil beam algorithm in MasterPlan, the reduced output variation should improve the accuracy of the calculated dose deposition.

3.1.5 Beam Quality

Assuming an accuracy of the water depth where the ion-chamber is positioned in the phantom of ± 0.1 mm and a dose variation with depth of 3 % per centimetre and that the uncertainty in the dosimeter reading relative to the beam monitor according to IAEA TRS-398 is 0.6 %. The total uncertainty (one standard deviation) will then be about 1.2 % (cf. Andreo, 1990) as the variation of stopping power between the two depths can be neglected (Andreo and Brahme, 1986).

The beam quality ($TPR_{20,10}$) was found to be 0.664 ± 0.008 for the flattening filter free beam. For previous measurements on a similar machine with a 6 MV beam with the flattening filter present, the beam quality was 0.681 ± 0.008 . This reflects the harder spectrum of the flattened 6 MV beam. The reported measure of beam quality for a 5 MV photon beam is 0.646 (BRJ Supplement 25, 1996). This is a somewhat softer beam than the flattening filter free beam. This suggest, as mentioned in Section 3.1.2, that in order to produce a flattening filter free beam with equal beam quality as a flattened beam, the energy of the initial electron beam has to be increased. The beam quality index used to derive the values in Table 3.2 must be considered less accurate than the $TPR_{20,10}$, mainly due to the fact that in Table 3.2 the values for the flattening filter free beam and the 6 MV beam were measured at a SSD of 90 and corrected for a SSD of 100 cm.

3.2 Monte Carlo Simulations

3.2.1 Benchmarking

The comparison between measured and simulated depth-dose curves and dose profiles showed only small variations for different simulated initial electron beams. In Table 3.3, the mean of the local dose differences between measured and calculated data for the different initial electron beams are presented. Based on visual comparisons of depth doses and dose profiles and the calculations presented in Table 3.3, the conclusion was that an initial electron beam with a mean energy of 6.3 MeV, Gaussian energy spread of 0.5 MeV (FWHM) and lateral spread of 1.1 mm (FWHM), had the best fit. Comparisons between measured and calculated data using this initial beam are presented for a depth-dose curve (Figure 3.9) and a profile (Figure 3.10). They show a maximum difference of about 2 % beyond the depth of maximum dose and within the field, respectively. This is not an optimal fit; however, considering the extent of this project it is satisfying.

It has been proposed that the radial intensity distribution and the energy distribution do not pose any significant influence on photon beams without flattening filter (De Smedt *et al.*, 2005). This was in agreement with the calculations in this study.

A comparison between measured and calculated flattening filter free dose profiles at depths of 1.5, 5, 10 and 20 cm in water is shown in Figure 3.11 (For flattened profiles, see Figure A.3 in the Appendix). The calculated profiles are normalised to the dose value between off-axis positions of -2.5 and 2.5 cm for the calculated profile at a depth of 10 cm and the measured profiles are normalised to the value between -2.5 and 2.5 cm for the calculated profile at their respective depth.

Table 3.3 *The mean local dose difference for various incident electron beams normalised to the values for the beam with mean energy of 6.3 MeV, energy distribution of 0.5 MeV and radial distribution of 1.1 mm. The mean local dose difference is calculated as the total mean of the dose differences between each calculated point and measurements. Reported differences are for the complete dose profile, central ± 8.75 cm of the dose profile and the complete depth-dose curve. The field size is 20×20 cm² and the profiles are calculated at a depth of 10 cm in water with a SSD of 90 cm.*

Initial electron parameters			Mean value of local dose difference normalised to the initial beam with mean energy 6.3 MeV,		
Mean energy [MeV]	FWHM of energy distribution [MeV]	FWHM of lateral distribution [mm]	Complete profile	Central ± 8.75 cm of profile	Depth dose
6.2	0.5	1.1	1.14	1.40	1.20
6.2	1	1.1	1.18	1.36	1.16
6.3	0.5	1.1	1	1	1
6.3	1	1.1	1.14	1.23	0.86
6.4	0.5	1.1	1.07	1.17	1.02
6.4	1	1.1	1.34	1.63	0.91
6.4	0.5	4	1.37	1.41	0.90
6.4	1	4	1.58	1.81	0.90
6.5	0.5	1.1	1.31	1.53	0.84
6.5	1	1.1	1.93	2.71	1.35

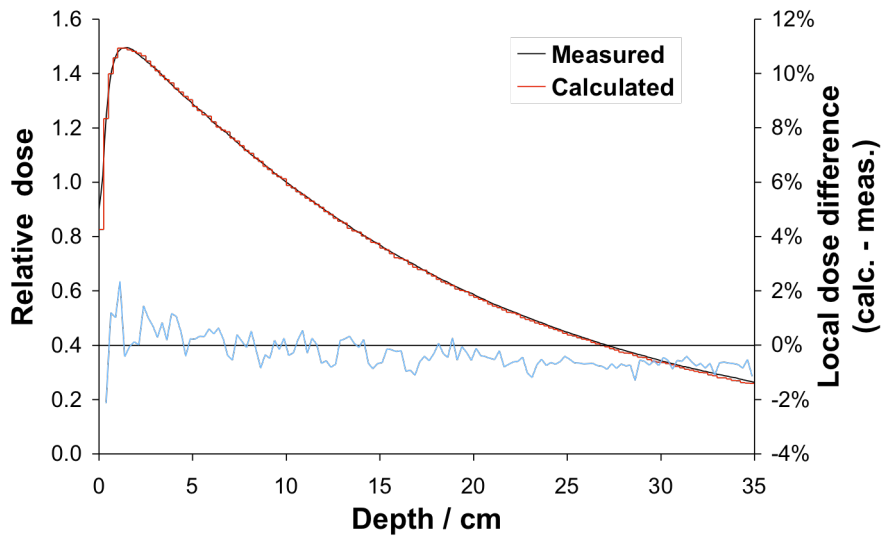


Figure 3.9 Comparison of calculated and measured depth-dose curves for a field size of $20 \times 20 \text{ cm}^2$ with SSD 90 cm. For the calculated depth dose an incident electron beam with a mean energy of 6.3 MeV, Gaussian shaped energy distribution with energy at FWHM of 0.5 MeV and radial intensity distribution FWHM of 1.1 mm was used. The depth-dose curves are normalised to the dose value at a depth of 10 cm. The calculated uncertainty in each point is below 0.5 % (1 S.D.) within the radiation field.

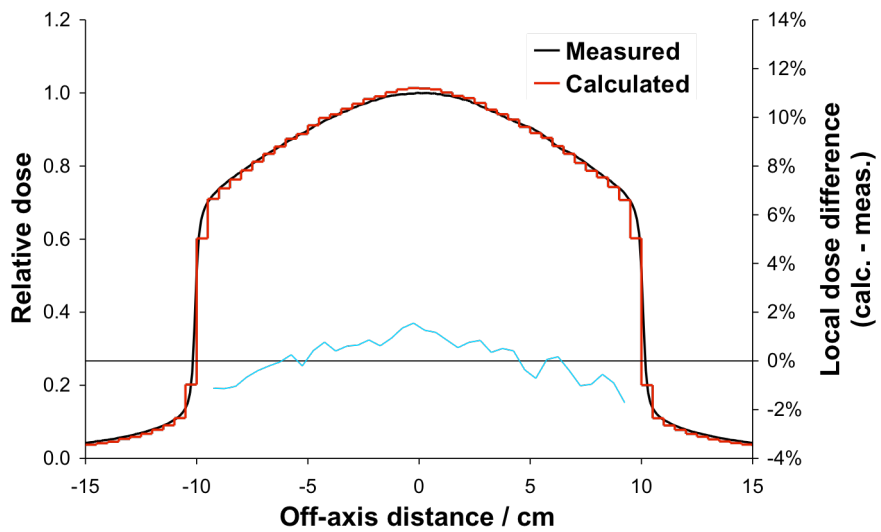


Figure 3.10 Comparison of local dose difference between calculated and measured dose profiles at 10 cm depth in water with a SSD of 90 cm and a field size of $20 \times 20 \text{ cm}^2$. The incident electron beam is the same as in Figure 3.9. The values of the calculated profile are normalised to the mean value between off axis point of -25 to 25 mm and the measured profile is normalised to the dose value at the central axis. The calculated uncertainty in each point is below 0.5 % within the radiation field.

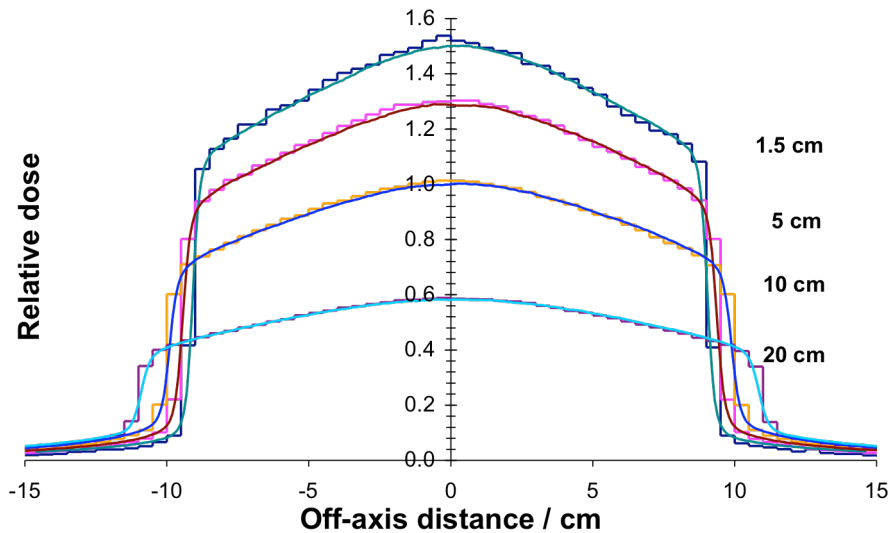


Figure 3.11 Measured and calculated dose profiles at four different depths: 1.5, 5, 15 and 20 cm. The measured profiles are normalised to the dose value between off-axis point at -2.5 cm and 2.5 cm of the calculated profile at each depth and the calculated profiles are normalised to the dose value at the same interval for the dose profile at 10 cm depth.

3.2.2 Photon Fluence

The photon spectra, or photon fluence distribution in energy, presented in Figure 3.12, were extracted at a depth of 10 cm in water with a field size of $10 \times 10 \text{ cm}^2$. A comparison of the two irradiation modes shows a larger fraction of low-energy photons in the flattening filter free mode. The differences in spectral changes at an off-axis distance are small for both with and without filter but slightly larger for the flattened beam.

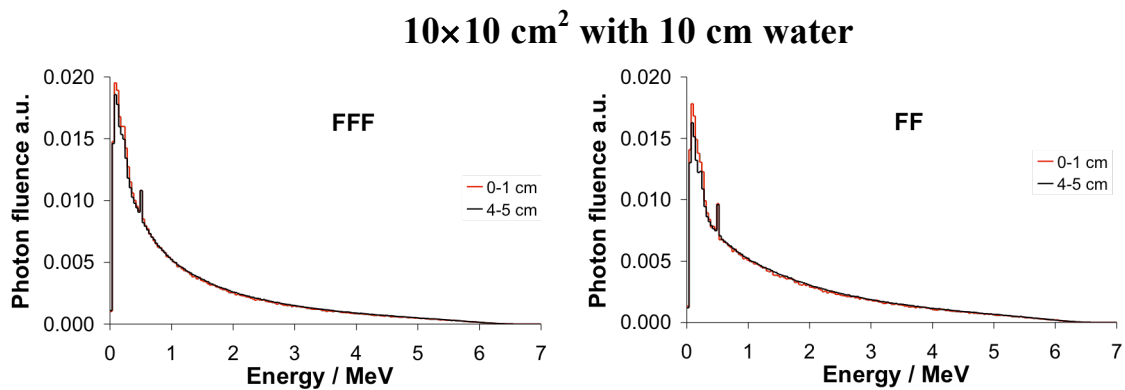


Figure 3.12 Monte Carlo calculated photon spectra normalised per unit total fluence, extracted from a plane perpendicular to the central axis at a depth of 10 cm in water with a SSD of 100 cm and a field size of $10 \times 10 \text{ cm}^2$. The spectral information is averaged in a circle centred at the central axis with a radius of 1 cm (red line) and at an off-axis distance of 4-5cm (black line) One diagram for the flattened beam (left) and one for the unflattened beam (right). The error in each point is about 2 %.

40×40 cm² at SSD 100 cm free in air

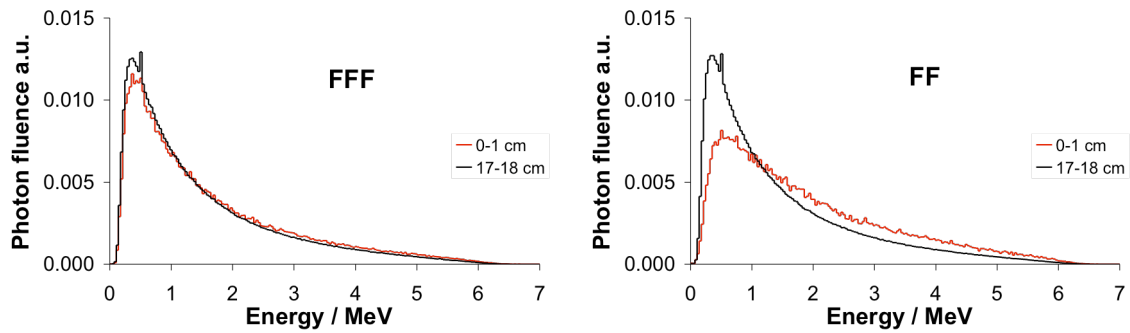


Figure 3.13 Monte Carlo calculated photon spectra normalised per unit total fluence, extracted from a plane perpendicular to the central axis with a SSD of 100 cm and a field size of 40×40 cm². The spectral information is averaged in circles centred at the central axis with a radius of 1 cm (red line) and at an off-axis distance of 17-18 cm (black line). One diagram for the flattened beam (left) and one for the unflattened beam (right). The error in each point is about 2 %.

Figure 3.13 was generated using the phase space for the 40×40 cm² field, where the spectra are calculated in air at a SSD of 100 cm. In this figure it is clear that the low energy part of the flattened spectra is increased close to the field edge, i.e. at an off-axis distance of 17-18 cm. The spectra from flattening filter free and the flattened beams are almost identical at the field edge, where the fluence weighted mean energy (\bar{E}) was 1.45 MeV for the flattened beam and 1.47 MeV for the flattening filter free beam. At this off-axis distance, the primary photons will pass through less material in the flattening filter than in the copper plate. This effect could be levelled by the increased amount of scattered radiation in the field for the flattened beam, increasing the low energy portion of the spectrum, and hence give rise to a similar spectrum for the two beams at this off-axis distance. However, at the central axis the difference in spectral shape between the two modes are quite large and \bar{E} was 1.90 MeV and 1.60 MeV for the flattened and unflattened beam, respectively.

The mean energies averaged over the entire fields are presented in Table 3.4. For the smaller field size, there is a larger difference between the two beams. The strongest reason for this is probably the different field sizes used in the investigation.

Table 3.4 Mean photon energy, \bar{E} , averaged over the entire field for the 10×10 cm² field at 10 cm depth in water with SSD 100 cm and for the 40×40 cm² field free in air at a SSD of 100 cm.

Field size (cm ²)	Mean energy FF (MeV)	Mean energy FFF (MeV)
10×10	1.53	1.44
40×40	1.52	1.49

The photon fluence variation across the treatment field, along a line parallel to the MLC leaves from the central axis to the field edge, is presented in Figure 3.14. At the central axis the fluence is 1.99 times higher for the flattening filter free beam, however, considering the entire $40 \times 40 \text{ cm}^2$ field, the photon fluence is only 1.13 times higher in flattening filter free mode, see Table 3.5. One of the reasons for this is that at an off-axis distance greater than about 15 cm, the cone shaped flattening filter attenuates less photons than the copper plate.

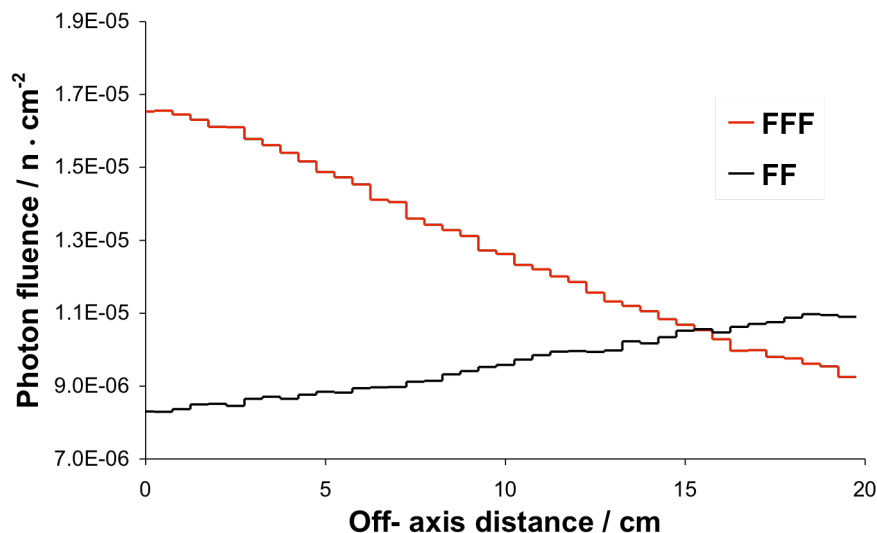


Figure 3.14 Photon fluence distribution per incident electron, n , across the field for a field size $40 \times 40 \text{ cm}^2$. The phase space used was extracted free in air at a SSD of 100 cm. The fluence is averaged in rectangular bins that were 0.5 cm large in the axis of interest and 2 cm wide in order to achieve a calculated uncertainty below 0.5 %.

At a depth of 10 cm in water, the fluence at the central axis was found to be 2.02 times higher for the flattening filter free beam for a field size of $10 \times 10 \text{ cm}^2$. In Figure 3.15, the relative variation of fluence across the field is shown. Because of the photon attenuation and scatter in water, the off-axis softening causes the fluence to be reduced with off-axis distance even for the flattened beam, in contrast to the $40 \times 40 \text{ cm}^2$ field calculated free in air. Averaged over a circle with a radius of 5 cm and its centre at the central axis, replacing the flattening filter with the copper plate increased the fluence 1.91 times (Table 3.5).

Photon fluences per initial electron are presented in Table 3.5. Three different positions were investigated: the downstream surface of the filters, at SSD 100 cm free in air and at 10 cm depth in water with a SSD of 100 cm. For the latter the field size was $10 \times 10 \text{ cm}^2$ and for the other two it was $40 \times 40 \text{ cm}^2$.

The photon fluence per initial electron at the downstream surface of the filters is 6 % lower when the copper filter is used. The fluence presented is averaged over the entire area of the filter and the cause of the lower average fluence for the flattening filter free beam is a steep drop at a distance of 0.5 cm from the edge of the filter located outside the primary photon beam.

If only the area covered by the primary beam is considered, the fluence is increased by 2 % for the flattening filter free beam. This could be an indication of a lower amount of scattered radiation for unflattened beams, as the photon fluence outside the beam is reduced. At the central axis the number of photons per initial electron is 55 % higher when the flattening filter free beam is used.

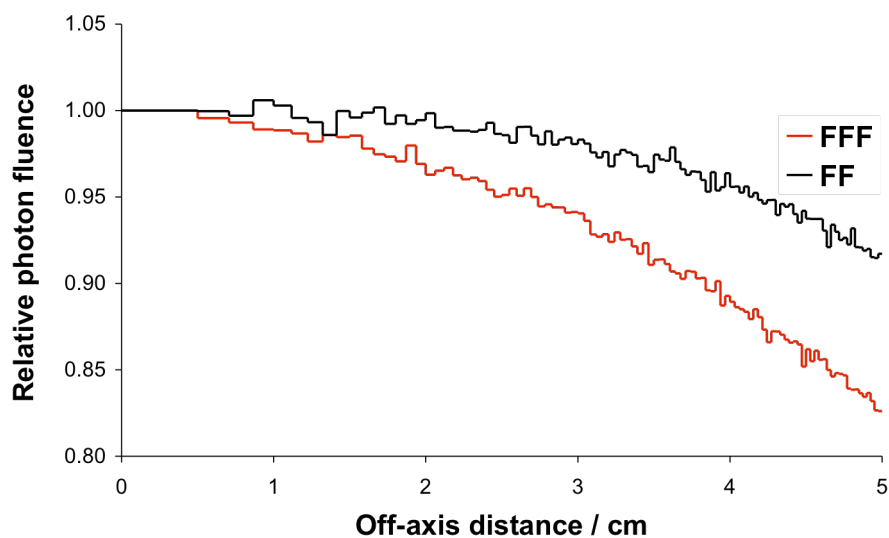


Figure 3.15 The photon fluence variation at a depth of 10 cm in water, normalised to the central-axis values.

Table 3.5 Photon fluences per initial electron at the downstream surface of the filter, at a SSD of 100 cm for a $40 \times 40 \text{ cm}^2$ field and at 10 cm depth in water for a $10 \times 10 \text{ cm}^2$ field. The photon fluences are averaged in circles covering the entire filters, and with a radius of 20 and 5 cm, respectively, for the 40×40 and $10 \times 10 \text{ cm}^2$ fields.

Field size	$10 \times 10 \text{ cm}^2$	$40 \times 40 \text{ cm}^2$	$40 \times 40 \text{ cm}^2$
	Photon fluence at 10 cm depth with SSD 100 cm [cm^{-2}]	Photon fluence in air at SSD 100 cm [cm^{-2}]	Photon fluence at backside of the filter [cm^{-2}]
FF	$1.16 \cdot 10^{-5}$	$1.01 \cdot 10^{-5}$	$4.67 \cdot 10^{-4}$
FFF	$2.22 \cdot 10^{-5}$	$1.14 \cdot 10^{-5}$	$4.39 \cdot 10^{-4}$

3.2.3 Dose Output

One of the suggested advantages of a flattening filter free photon beam is the increased dose output, which could reduce the beam-on time for IMRT treatments. In Figure 3.16, the ratio of dose per initial electron at points between the central axis and the field edge of a flattening filter free and a flattened beam for a $20 \times 20 \text{ cm}^2$ field is shown. The profiles were calculated at a depth of 10 cm in water with a SSD of 90 cm. In the Appendix the dose output as a function of off-axis distance and as a function of depth are shown in Figure A.1-A.2.

The output is, as expected, higher for the flattening filter free beam. The reduction of material in the beam reduces the amount of primary photons that is scattered and absorbed in the flattening filter. At the central axis the dose per initial electron is 1.75 times higher for the flattening filter free beam. This is lower than a reported output ratio of 2.13 for the same field size for an Elekta SL-25 by Mesbahi, *et al.* (2007). This difference can be explained by the lack of copper plate in the beam line in that study. Although, studies on a Varian 21EX and 2100 showed an increased output of about 2.3 for the unflattened beam when a 2 mm thick copper plate was added in the beam line in the flattening filter free mode (Vassiliev, *et al.*, 2006a, Vassiliev, *et al.*, 2006b).

The increase in output for the flattening filter free beam can be an advantage when treating patients with the IMRT technique. However, an increased dose rate does not automatically reduce the overall time required to deliver one fraction of the treatment. If treating with large fractional doses, e.g. hypo fractionation and radiosurgery, the effect should be most of use.

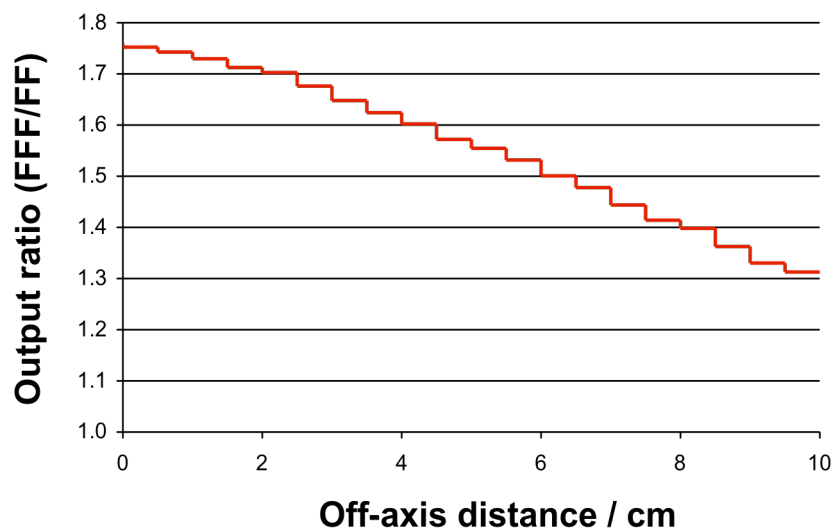


Figure 3.16 Output ratio for flattening filter free and a flattened beam at a depth of 10 cm of water with a SSD of 90 cm and a field size of 20×20 cm². The uncertainty in each point is below 0.5 %.

3.2.4 Angular distribution

The angular distribution of the photons in the entire 40×40 cm² field at a SSD of 100 cm is shown in Figure 3.17. There is a larger amount of photons with angles up to about 10 degrees relative to the beam axis, when radiating in flattening filter free mode. This angle represents an off-axis distance of about 18 cm, and the higher proportion of photons with smaller angles could indicate a higher amount of primary photons in the flattening filter free beam. For the angle interval between 10 and 30 degrees there are more photons from the flattened beam. This could be a reflection of the proportion of single or a few times scattered photons in the beam, which should be higher in the flattened beam. Photons with larger angles ($\geq 30^\circ$) could then represent multiple scattered photons, which are in quite similar amounts for the two beams, although there are a few more photons with these angles for the flattening filter free beam. This increased amount could be due to the lower energy and hence larger cross-section for photon interaction in the air for the unflattened beam.

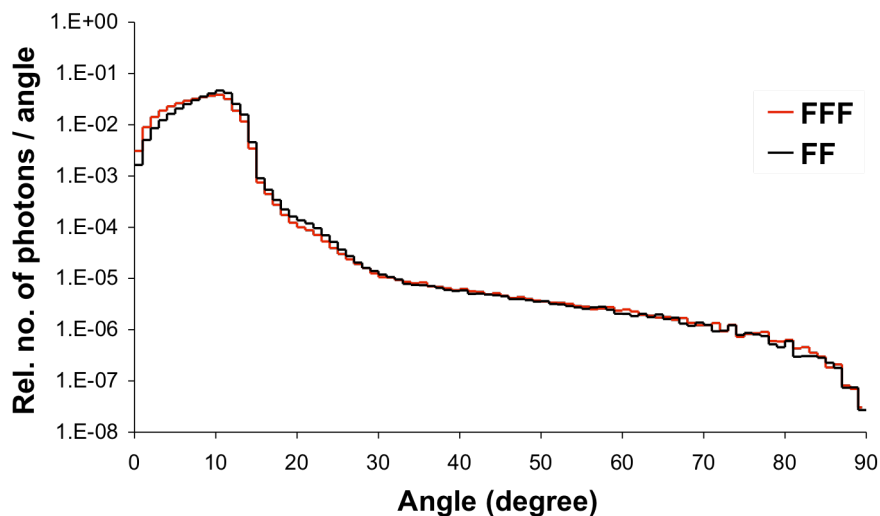


Figure 3.17 Angular distribution of photons over the entire $40 \times 40 \text{ cm}^2$ field impinging on the scoring plane positioned free in air at a SSD 100 cm. The photon angle is defined as the angle between the photon direction and the central axis. The calculated uncertainty is below 0.5 % for angles up to 25 degrees and below 2 % up to 40 degrees (N.B the logarithmic scale).

3.2.5 Photon Origin

The last interaction points of the photons in the phase space acquired at a SSD of 100 cm free in air, over the entire field size of $40 \times 40 \text{ cm}^2$, are displayed in Figure 3.18. Different components in the accelerator head can easily be distinguished, starting with the target at $z=0 \text{ cm}$, where the very large amount of photons originating from this position is not entirely displayed. After the target there is a slope until $z \approx 12 \text{ cm}$, representing photons from the primary collimators. The three peaks thereafter are photons from the filter, monitor chamber and backscatter plate after which there is a gap to the secondary collimators, starting with the MLC and continues with the back-up and outer jaws. The peak after the collimators at $z \approx 53 \text{ cm}$ is photons having their last interaction in the Mylar window.

In Table 3.6, the ratios of particles having their last interaction in different areas of the accelerator head are presented for the flattening filter free and the flattened beams.

By using the LATCH option, where it is possible to extract if a particle at some stage in its “history” interacted in a specific region, it was found that there is a reduction of $32 \pm 6 \%$ of photons that interacted in the copper filter compared to the flattening filter. The reduction of photons having their *last* interaction in the flattening filter is about 21 %.

As discussed in Section 3.1.3, the reduction of scattered radiation, which is about 12 % for a $40 \times 40 \text{ cm}^2$ field, could improve the dose calculations in treatment planning systems.

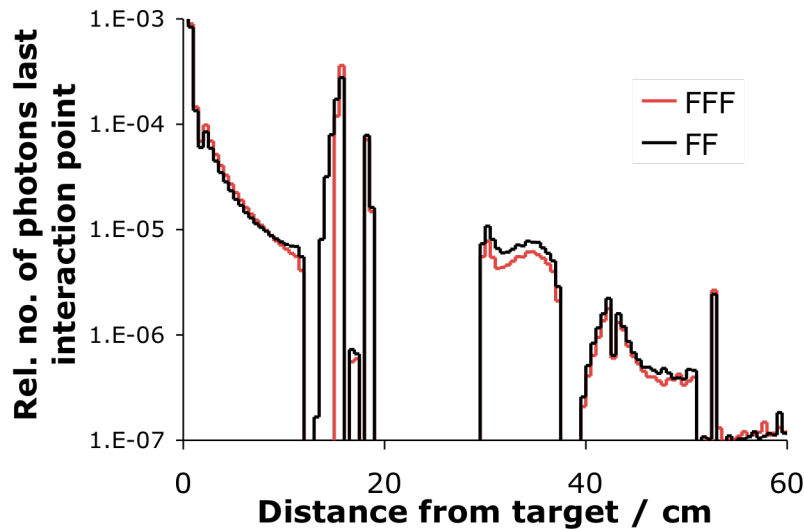


Figure 3.18 Distribution of the last interaction points for photons along the z-axis for the $40 \times 40 \text{ cm}^2$ field free in air at a SSD of 100 cm. For values within the position of an accelerator component the calculated uncertainty is below 1 % (N.B the logarithmic scale).

Table 3.6 Percentages of the total amount of photons, having their last interaction at the same distance interval along the z-axis, and reaching the scoring plane with (FF) and without (FFF) a flattening filter in the beam line. The scoring plane is positioned in air at a SSD of 100 cm and the field size is $40 \times 40 \text{ cm}^2$. The calculated uncertainty is about 5 % for the target, 0.1 % for the filter and primary collimators, below 0.02 % for the collimators and 0.2 % for the total amount of scatter.

Accelerator Component z-direction interval in brackets	FF (%)	FFF (%)	FFF/FF (%)
Target (0-1.5 cm)	93.73	94.47	0.8
Primary Collimators (1.5-12 cm)	2.33	2.43	4.3
Filter (13-16 cm)	2.75	2.16	-21.5
Collimators (29,5-37.5 cm, 39.5-51 cm)	0.61	0.44	-27.9
Total amount of scatter (1.5-100 cm)	6.27	5.53	-11.8

Variation of HVL with Off-Axis Angle

As previously mentioned (and shown in Section 3.1.1), the beam quality varies less across the field when the flattening filter is removed. In Figure 3.19, the half-value layer as a function of off-axis angle is shown. The variation between the HVL at the central axis and at the field edge is reduced more than 3.3 times by replacing the flattening filter with the copper plate. It is worth to notice that the HVL is equal for the two beams at an off-axis angle between 9 and 10 degrees, which corresponds to an off-axis distance of about 17 cm, as previously mentioned in Section 1.2.2.

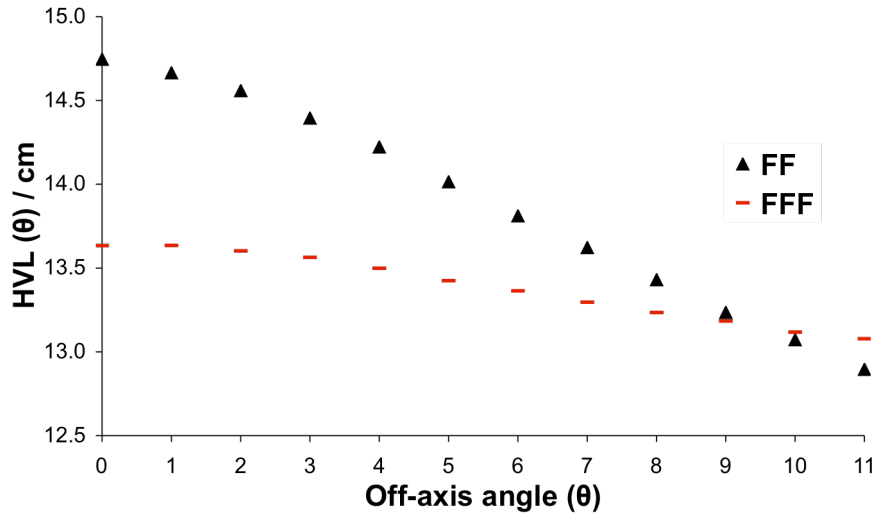


Figure 3.19 Calculated values of the variation of HVL with off-axis angle. The field size used is $40 \times 40 \text{ cm}^2$ and the SSD is 100 cm.

In Figure 3.20, the relative values of the HVL are presented and for comparison the fit from Taylor, *et al.* (1998) is included. This curve fits well with the calculated ratio for the flattened beam. A fit to the calculated HVL-values for the flattening filter free beam is also included and just as eq. 6 for FF beams it is a third-degree polynomial:

$$HVL/HVL(\theta) = 1 + 2.76 \cdot 10^{-6} \theta + 7.31 \cdot 10^{-4} \theta^2 + 3.78 \cdot 10^{-5} \theta^3 \quad (8)$$

When calculating dose deposition with an algorithm that corrects for off-axis softening, for example MasterPlan CC, using a flattening filter free beam it will be over-corrected if the off-axis softening from Taylor, *et al.* (1998) is used. If the MasterPlan PB algorithm is used, the spectra of monoenergetic pencil beams used will more accurately represent the actual photon spectra over the entire treatment field, if a flattening filter free beam is used.

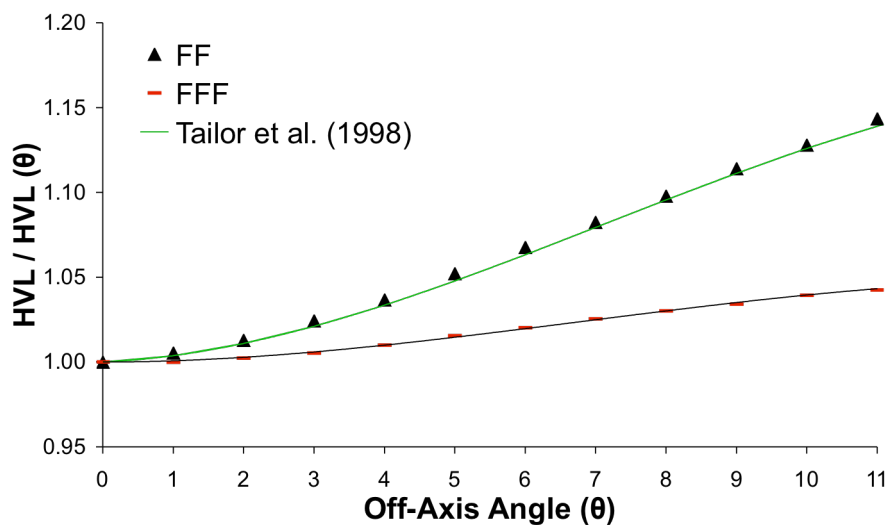


Figure 3.20 Variation of the relative half-value layer as a function of off-axis angle for flattened (black triangles) and unflattened beams (red bars). Also included in the figure is the fit from Taylor, *et al.* (1998) derived from measurements on several different linacs (green line).

4 Conclusions and Future Work

Measurements and Monte Carlo simulations have been performed, using an Elekta Precise medical linear accelerator operating with and without a flattening filter in the beam line. A Monte Carlo model has successfully been developed and verified, using measured data. The measured and computer-simulated data has been used to evaluate the basic properties of the flattening filter free beam and comparisons of this beam with a conventional flat beam has been performed.

It was found that removing the flattening filter increased the dose rate by 1.75 times at the central axis. This increase reflects the reduction of photons absorbed in the copper plate compared to the flattening filter. The overall reduction of scattered radiation from the accelerator head was found to be about 12 % for a 40×40 cm² field. This is also reducing the variation in output for different field sizes. The reduced amount of scatter along with the higher dose rate at the central axis could reduce the out-of field dose.

The softer spectrum of the flattening filter free beam is similar to a photon beam of a conventional accelerator with a nominal energy between 5 and 6 MV. The variation of beam quality across the field for the flattening filter free beam is reduced by more than a factor of 3 compared to a conventional flattened beam. It has also been shown that this property reduces the variation of the shape of dose profiles at different depth in a water phantom. The penumbral width was found to be slightly smaller for the flattening filter free beam.

The properties of the flattening filter free beam can help reducing the dose calculation uncertainties in treatment planning systems since the corrections for scattered radiation, off-axis softening and dose profile variations with depth are less important when calculating dose deposition for a flattening filter free beam. The characteristics of the beam is suitable for treatments with smaller fields, e.g. in IMRT, where a better dose distribution may be achieved.

For the future, investigation of electron properties at various positions of the accelerator head, especially at the monitor chamber, is needed. One of the main purposes for the copper plate, stated by Elekta, is to produce electrons to facilitate the steering of the beam. One question to seek an answer for would be if it's possible to construct a thinner copper plate and still get enough electrons for the monitor chamber. Monte Carlo studies of a higher energy flattening filter free beam (10 MV) and a flattening filter free beam producing a 6 MV photon beam which are being measured at the Allgemeines Krankenhaus in Vienna, Austria, is also a project for the future.

Acknowledgements

Elekta medical systems for setting up the flattening filter free beam and providing the parts needed for the delivery of this beam. Elekta has also provided the accelerator head data needed for the MC simulations.

The MC simulations have been performed on 3.2 GHz personal computers funded by Lund University Hospital Research funds and on a Linux cluster at Rigshospitalet, Copenhagen, Denmark, which is partly funded by the Toyota Foundation.

I would like to thank my supervisors, Elinore Wieslander, Tommy Knöös, Brendan McClean and Patrick McCavana for their guidance and for giving me the opportunity to do this work.

I would also like to thank the staff at the radiotherapy department at St. Luke's hospital, Dublin, Ireland and at radiophysics at Lund University Hospital for answering my many questions and always being prepared to help.

Thank you Elin Dalaryd and Magnus Jonsson for your support.

Finally, I would like to thank Sacha af Wetterstedt for being a great colleague and friend during our measurements in Dublin.

References

- Andreo, P.**, 1990, *Uncertainties in dosimetric data and beam calibration*, Int. J. Radiat. Oncol. Biol. Phys., 19:5, 1233-1247
- Andreo, P. and Brahme, A.**, 1986, *Stopping power data for high-energy photon beams*, Phys. Med. Biol., 31:8, 839-858
- Berger, M. J.**, 1963, *Monte Carlo calculation of the penetration and diffusion of fast charged particles.*, Methods in Comput. Phys., 1:135-215
- The British Journal of Radiology**, 1996, *Central axis depth dose data for use in radiotherapy*, Brit. J. Radiol. Supplement No. 25.
- De Smedt, B., Reynaert, N., Flachet, F., Coghe, M., Thompson, M. G., Paelinck, L., Pittomvils, G., De Wagter, C., De Neve, W. and Thierens, H.**, 2005, *Decoupling initial electron beam parameters for Monte Carlo photon beam modelling by removing beam-modifying filters from the beam path*, Phys. Med. Biol., 50:24, 5935-5951
- Fix Michael, K., Stampanoni, M., Manser, P., Born Ernst, J., Mini, R. and Ruegsegger, P.**, 2001, *A multiple source model for 6 MV photon beam dose calculations using Monte Carlo*, Physics in Medicine and Biology, 46:5, 1407-1427
- Fix, M. K., Stampanoni, M., Manser, P., Born Ernst, J., Mini, R. and Ruegsegger, P.**, 2001, *A multiple source model for 6 MV photon beam dose calculations using Monte Carlo*, Phys. Med. Biol., 46:5, 1407-1427
- Fu, W., Dai, J., Hu, Y., Han, D. and Song, Y.**, 2004, *Delivery time comparison for intensity-modulated radiation therapy with/without flattening filter: a planning study*, Phys. Med. Biol., 49:8, 1535-1547
- Hanson, W. F., Berkley, L. W. and Peterson, M.**, 1980, *Off-axis beam quality change in linear accelerator x-ray beams*, Med. Phys., 7:2, 145-146
- Hubbell, J. M. and Seltzer, S. M.**, 1995, *Tables of x-ray mass attenuation coefficients and mass energy-absorption coefficients from 1 keV to 20 keV for elements $z = 1$ to 92 and 48 additional substances of dosimetric interest.*, Ionizing Radiation Division, Physics Laboratory National Institute of Standards and Technology, Gaithersburg, MD 20899 (<http://www.nist.gov>)
- IAEA International Atomic Energy Agency**, 2000, *Absorbed Dose Determination in External Beam Radiotherapy*, Technical Report Series no. 398, IAEA, Vienna
- Jeraj, R., Mackie, T. R., Balog, J., Olivera, G., Pearson, D., Kapatoes, J., Ruchala, K. and Reckwerdt, P.**, 2004, *Radiation characteristics of helical tomotherapy*, Med. Phys., 31:2, 396-404
- Kawrakow, I.**, 2000, *Accurate condensed history Monte Carlo simulation of electron transport. I. EGSnrc, the new EGS4 version*, Med. Phys., 27:3, 485-498
- Kawrakow, I. and Rogers, D. W. O.**, 2002, *The EGSnrc Code System: Monte Carlo Simulation of Electron and Photon Transport*, NRCC Report PIRS-701

Kawrakow, I., Rogers, D. W. O., Walters, B., 2004, *Large efficiency improvements in BEAMnrc using directional bremsstrahlung splitting*, Med. Phys. 31:10, 2883-2898

Knöös, T., Rosenschöld, P. M. a. and Wieslander, E., 2007, *Modelling of an Orthovoltage X-ray Therapy Unit with the EGSnrc Monte Carlo Package*, Journal of Physics: Conference Series, 74:021009

Kry, S. F., Titt, U., Pönisch, F., Vassiliev, O. N., Salehpour, M., Gillin, M. and Mohan, R., 2007, *Reduced Neutron Production Through Use of a Flattening-Filter-Free Accelerator*, Int. J. Radiat. Oncol. Biol. Phys., 68:4, 1260-1264

Lee, P. C., 1997, *Monte Carlo simulations of the differential beam hardening effect of a flattening filter on a therapeutic x-ray beam*, Med. Phys., 24:9, 1485-1489

Lovelock, D. M., Chui, C. S. and Mohan, R., 1995, *A Monte Carlo model of photon beams used in radiation therapy*, Med. Phys., 22:9, 1387-1394

Lutz, W. R. and Larsen, R. D., 1984, *The effect of flattening filter design on quality variations within an 8-MV primary x-ray beam*, Med. Phys., 11:6, 843-845

Ma, C. M. and Rogers, D. W. O., 1998, *BEAMDP as a General-Purpose Utility*, NRCC Report PIRS-0509(E)

Mesbahi, A., 2007, *Dosimetric characteristics of unflattened 6 MV photon beams of a clinical linear accelerator: a Monte Carlo study*, Appl. Radiat. Isot., 65:9, 1029-1036

Mesbahi, A., Mehnati, P., Keshtkar, A. and Farajollahi, A., 2007, *Dosimetric properties of a flattening filter-free 6-MV photon beam: a Monte Carlo study*, Radiat. Med., 25:7, 315-324

Metcalf, P., Kron, T. and Hoban, P., 2004, *The Physics of Radiotherapy X-rays from Linear Accelerators*, Third printing, Medical Physics Publishing, Madison, Wisconsin, 0-944838-75-6

Nelson, W. R., Hirayama, H. and Rogers, D. W. O., 1985, *EGS4 code system*,

O'Brien, P. F., Gillies, B. A., Schwartz, M., Young, C. and Davey, P., 1991, *Radiosurgery with unflattened 6-MV photon beams*, Med. Phys., 18:3, 519-521

Oncentra MasterPlan Physics and Algorithms, REF 192.739ENG-00, Nucletron B.V., Veenendaal, The Netherlands

Pearson, D., Parsai, E. and Feldmeier, J., 2006, *SU-FF-T-223: Evaluation of Dosimetric Properties of 6 & 10 MV Photon Beams From a Liner Accelerator with No Flattening Filter*, Med. Phys., 33:6, 2099-2099

Pönisch, F., Titt, U., Vassiliev, O. N., Kry, S. F. and Mohan, R., 2006, *Properties of unflattened photon beams shaped by a multileaf collimator*, Med. Phys., 33:6, 1738-1746

- Robar, J. L., Riccio, S. A. and Martin, M. A.**, 2002, *Tumour dose enhancement using modified megavoltage photon beams and contrast media*, Phys. Med. Biol., 47:14, 2433-2449
- Rogers, D. W. O. and Bielajew, A. F.**, 1990, *Chapter 5 of The Dosimetry of Ionizing Radiation*, Monte Carlo Techniques of Electron and Photon Transport for Radiation Dosimetry, Vol. 3, Academic Press, New York, 978-0124004016
- Rogers, D. W. O., Faddegon, B. A., Ding, G. X., Ma, C. M., We, J. and Mackie, T. R.**, 1995, *BEAM: a Monte Carlo code to simulate radiotherapy treatment units*, Med. Phys., 22:5, 503-524
- Rogers, D. W. O., Walters, B. and Kawrakow, I.**, 2005, *BEAMnrc Users Manual* NRCC Report PIRS-0509(A)revI
- Sheikh-Bagheri, D. and Rogers, D. W. O.**, 2002, *Sensitivity of megavoltage photon beam Monte Carlo simulations to electron beam and other parameters*, Med. Phys., 29:3, 379-390
- Spezi, E., Lewis, D. G. and Smith, C. W.**, 2002, *A DICOM-RT-based toolbox for the evaluation and verification of radiotherapy*, Phys. Med. Biol., 47:23, 4223-42232
- Taylor, R. C., Tello, V. M., Schroy, C. B., Vossler, M. and Hanson, W. F.**, 1998, *A generic off-axis energy correction for linac photon beam dosimetry*, Med. Phys., 25:5, 662-667
- Titt, U., Vassiliev, O. N., Pönisch, F., Dong, L., Liu, H. and Mohan, R.**, 2006a, *A flattening filter free photon treatment concept evaluation with Monte Carlo*, Med. Phys., 33:6, 1595-1602
- Titt, U., Vassiliev, O. N., Pönisch, F., Kry, S. F. and Mohan, R.**, 2006b, *Monte Carlo study of backscatter in a flattening filter free clinical accelerator*, Med. Phys., 33:9, 3270-3273
- Tsechanski, A., Bielajew, A. F., Faermann, S. and Krutman, Y.**, 1998, *A thin target approach for portal imaging in medical accelerators*, Phys. Med. Biol., 43:8, 2221-2236
- Tzedakis, A., Damilakis, J. E., Mazonakis, M., Stratakis, J., Varveris, H. and Gourtsoyiannis, N.**, 2004, *Influence of initial electron beam parameters on Monte Carlo calculated absorbed dose distributions for radiotherapy photon beams*, Med. Phys., 31:4, 907-913
- Walters, B., Kawrakow, I. and Rogers, D. W. O.**, 2002, *History by history statistical estimators in the BEAM code system*, Med. Phys., 29:12, 2745-2752
- Walters, B., Kawrakow, I. and Rogers, D. W. O.**, 2005, *DOSXYZnrc Users Manual*, NRCC Report PIRS-794revB
- Vassiliev, O. N., Kry, S. F., Kuban, D. A., Salehpour, M., Mohan, R. and Titt, U.**, 2007a, *Treatment-planning study of prostate cancer intensity-modulated radiotherapy with a Varian Clinac operated without a flattening filter*, Int. J. Radiat. Oncol. Biol. Phys., 68:5, 1567-1571

Vassiliev, O. N., Titt, U., Kry, S. F., Mohan, R. and Gillin, M. T., 2007b, *Radiation safety survey on a flattening filter-free medical accelerator*, Radiat. Prot. Dosimetry., 124:2, 187-190

Vassiliev, O. N., Titt, U., Kry, S. F., Pönisch, F., Gillin, M. T. and Mohan, R., 2006a, *Monte Carlo study of photon fields from a flattening filter-free clinical accelerator*, Med. Phys., 33:4, 820-827

Vassiliev, O. N., Titt, U., Pönisch, F., Kry, S. F., Mohan, R. and Gillin, M. T., 2006b, *Dosimetric properties of photon beams from a flattening filter free clinical accelerator*, Phys. Med. Biol., 51:7, 1907-1917

Verhaegen, F. and Seuntjens, J., 2003, *Monte Carlo modelling of external radiotherapy photon beams*, Phys. Med. Biol., 48:21, R107-164

Yu, M. K., Sloboda, R. S. and Murray, B., 1996, *Linear accelerator photon beam quality at off-axis point*, Med. Phys., 24:2, 233-239

Zefkili, S., Kappas, C. and Rosenwald, J. C., 1994, *On-axis and off-axis primary dose component in high energy photon beams*, Med. Phys., 21:6, 799-808

Zhu, T. C. and Bjärngard, B. E., 1994, *The head-scatter factor for small field sizes*, Med. Phys., 21:1, 65-68

Zhu, X. R., Kang, Y. and Gillin, M. T., 2006, *Measurements of in-air output ratios for a linear accelerator with and without the flattening filter*, Med. Phys., 33:10, 3723-3733

Appendix

Penumbral width

Table A.1 Penumbral width for measured profiles calculated using the method described in Section 2.2.2.1. The values for each field size and profile collimation are averaged between the two penumbras of each profile.

Field size	Penumbral width $P_{80/20}$ [mm]			
	MLC		Jaws	
	FF	FFF	FF	FFF
10×10	6.15	5.25	3.85	3.9
20×20	7.3	6.45	4.95	5.65

Dose Output

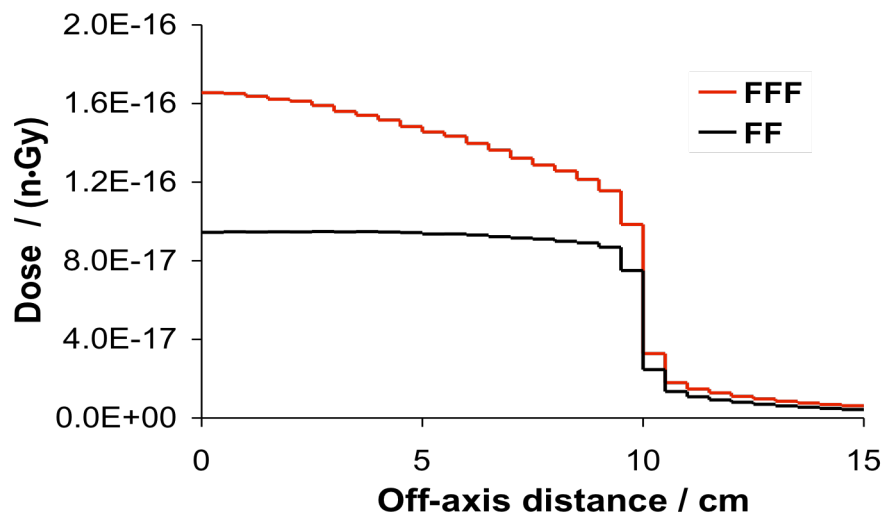


Figure A.1 Output variation per incident electron, n , with off-axis distance for a beam with and without a flattening filter in the beam line. The field size is $20 \times 20 \text{ cm}^2$ and the profiles are calculated at a depth of 10 cm with a SSD of 90 cm. The uncertainty in each point within the field is below 0.5 %.

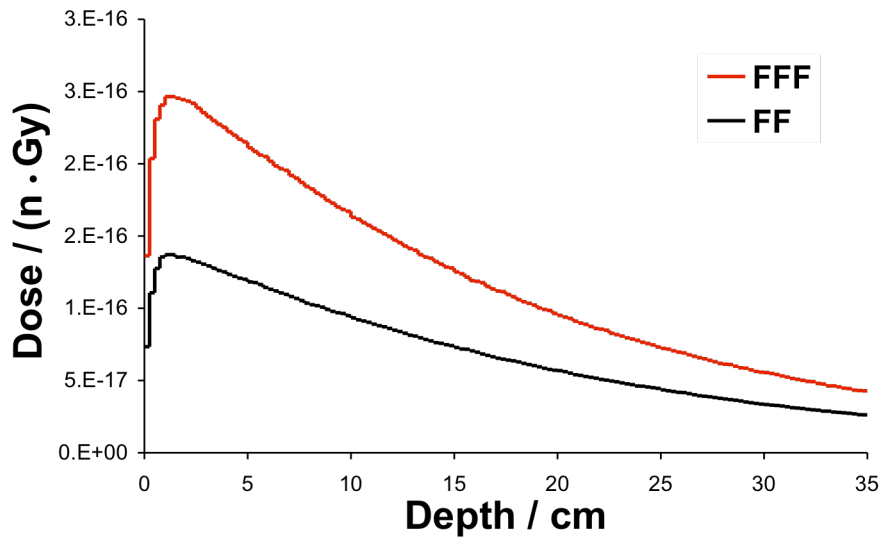


Figure A.2 Dose per incident electron, n , as a function of depth for a flattening filter free and a flattened beam. The field size used was $20 \times 20 \text{ cm}^2$ and the SSD was 90 cm. The uncertainty in each point is below 0.5 %.

Dose Profiles

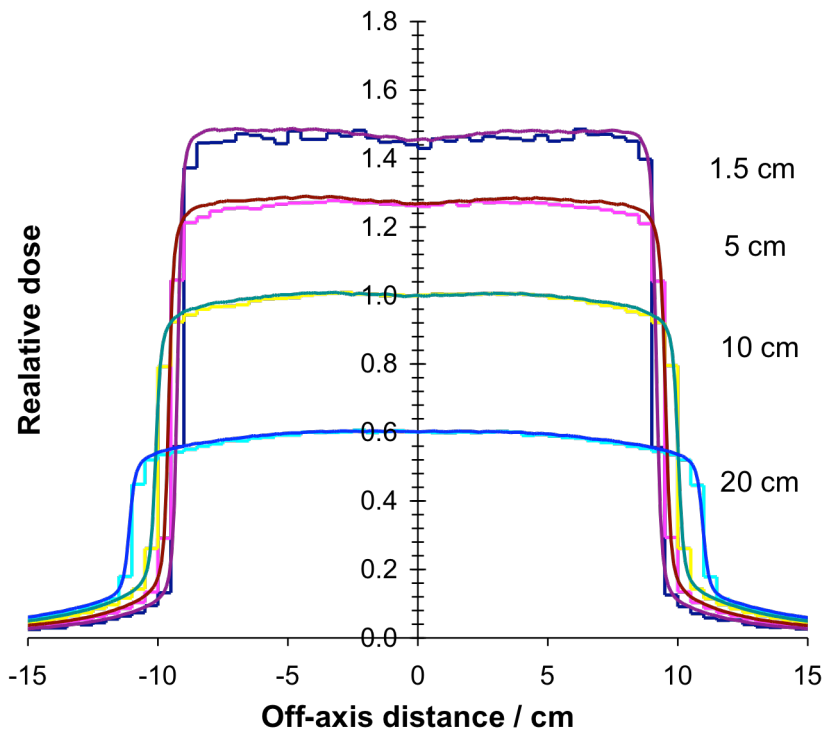


Figure A.3 Comparison of calculated and measured flattened profiles at four different depths: 1.5, 5, 10 and 20 cm with a SSD of 90 cm. The calculated profiles are normalised to the central-axis dose value at a depth of 10 cm and the measured profiles are normalised to the calculated relative dose value at the central axis at each depth. The uncertainties of the calculated dose values are below 0.5 % within the radiation field.

Photon Fluence

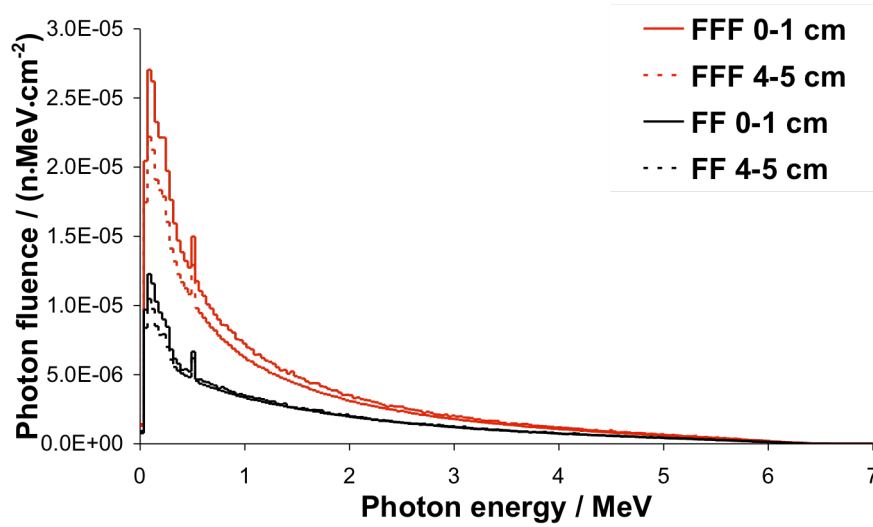


Figure A.4 Photon spectra averaged over two different areas of a phase space scored at a depth of 10 cm in water with a SSD of 100 cm and a field size of $10 \times 10 \text{ cm}^2$ for beams with and without flattening filter. The areas are defined as one circle around the central axis with a radius of 1 cm and one annulus with inner radius of 4 cm and outer radius of 5 cm, respectively. The uncertainty in each energy bin is below 1 %.

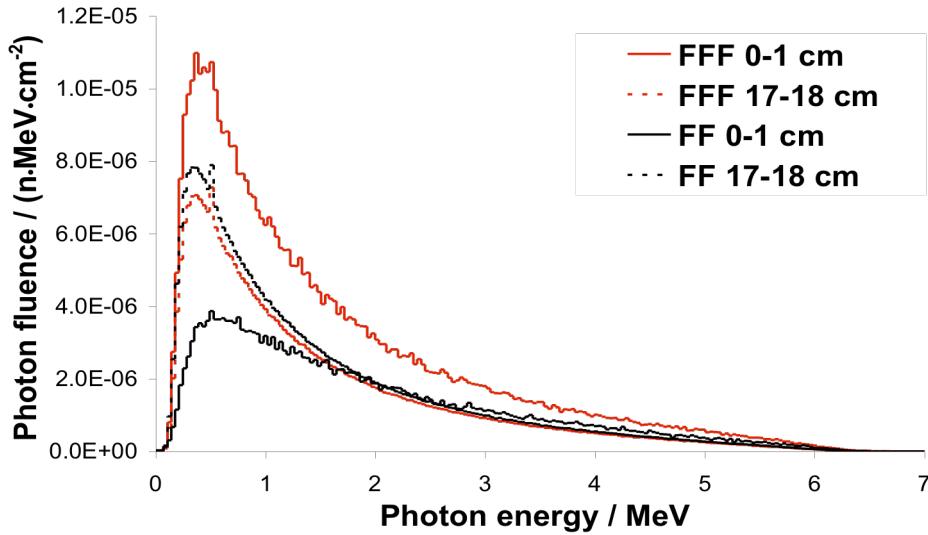


Figure A.5 Photon spectra per incident electron, n , averaged over two different areas of a phase space scored free in air at a SSD of 100 cm and a field size of $40 \times 40 \text{ cm}^2$ for beams with and without flattening filter. The areas are defined as one circle around the central axis with a radius of 1 cm and one annulus with inner radius of 17 cm and outer radius of 18 cm, respectively. The uncertainty in each energy bin is below 1 %.

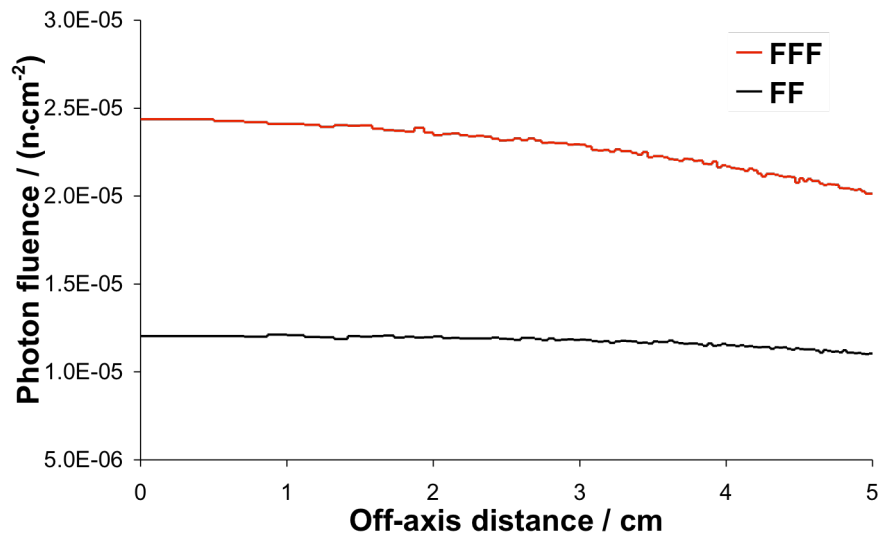


Figure A.6 Photon fluence across the $10 \times 10 \text{ cm}^2$ field at a depth of 10 cm in water with a SSD of 100 cm. The values are averaged over annuli with equal area and where the largest outer radius is 5 cm. The uncertainty in each point is below 0.5 %.

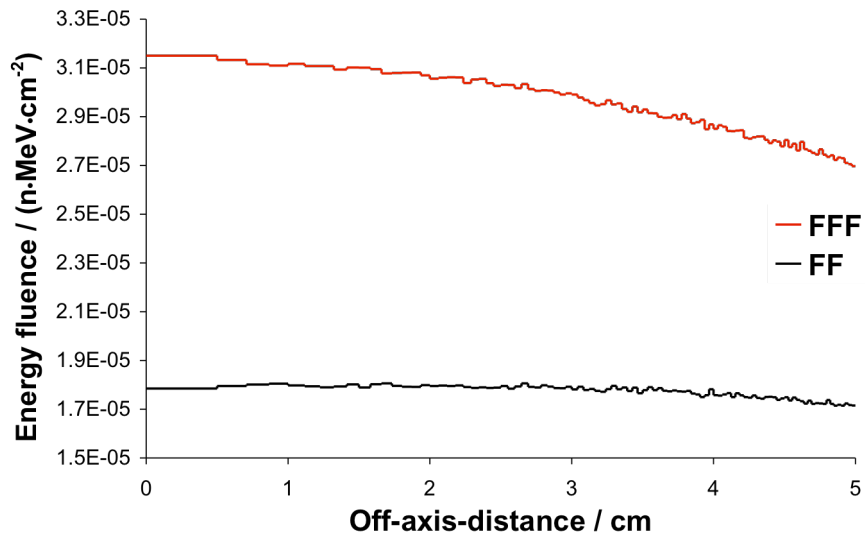


Figure A.7 Photon energy fluence calculated in annuli of equal area for the flattened and unflattened beams from the $10 \times 10 \text{ cm}^2$ field at a depth of 10 cm of water with a SSD of 100 cm. The calculated uncertainty in each point is below 0.5 %.

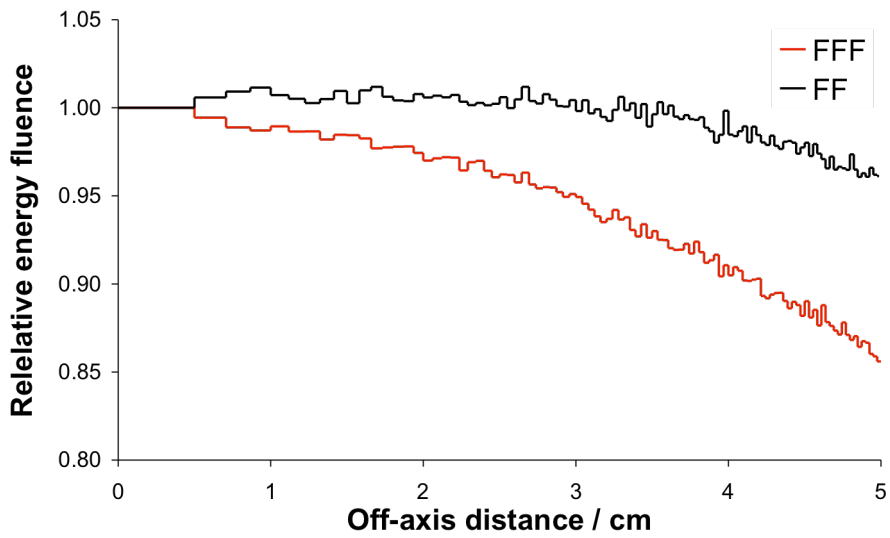


Figure A.8 Energy fluence, presented in Figure A.7, normalised to the central-axis value.

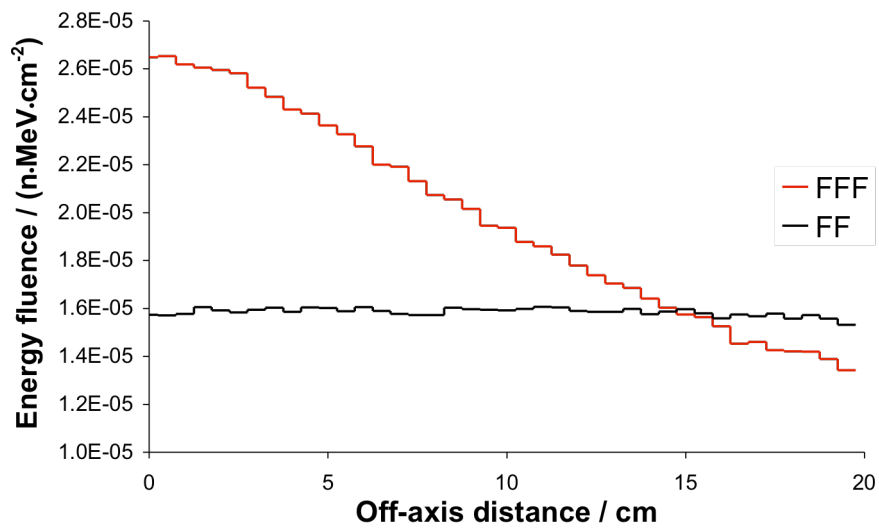


Figure A.9 Photon energy fluence for the $40 \times 40 \text{ cm}^2$ field. The energy fluence is averaged in $0.5 \times 2 \text{ cm}^2$ large rectangular bins and the estimated uncertainty in each bin is below 0.5 %.

Mean Energy of Photons

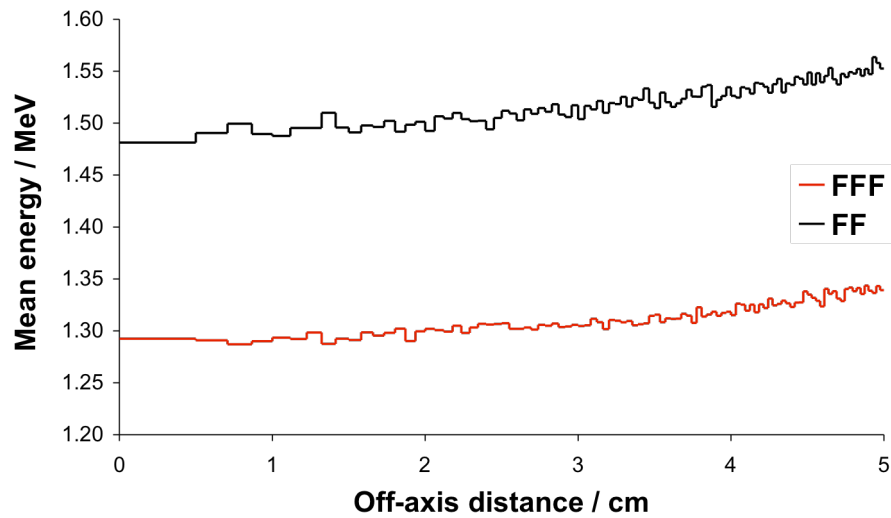


Figure A.10 Mean energy of photons in annuli with equal area for the $10 \times 10 \text{ cm}^2$ field at 10 cm depth in water with a SSD of 100 cm. The calculated uncertainty in each annulus is below 0.5 %.

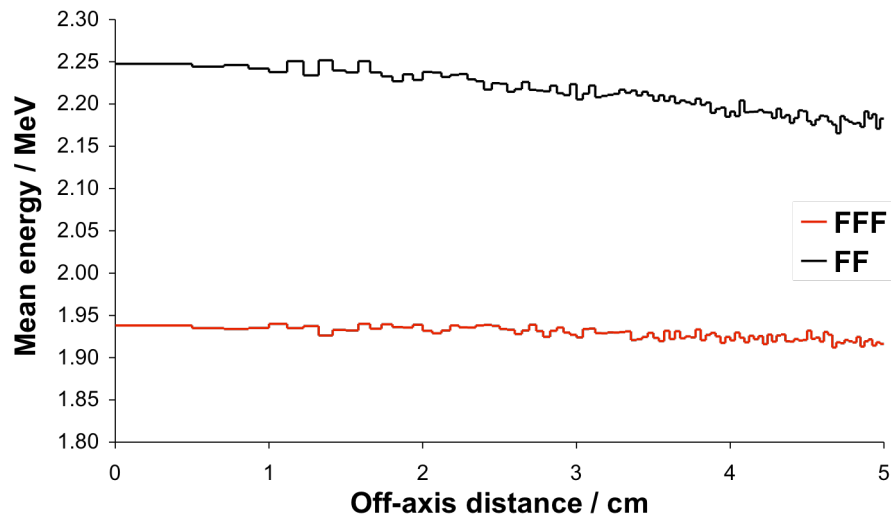


Figure A.11 Mean energy of the primary photons reaching a plane at 10 cm depth in water. The SSD is 100 cm and the field size is $10 \times 10 \text{ cm}^2$. The calculated uncertainty in each annulus is below 0.5 %.

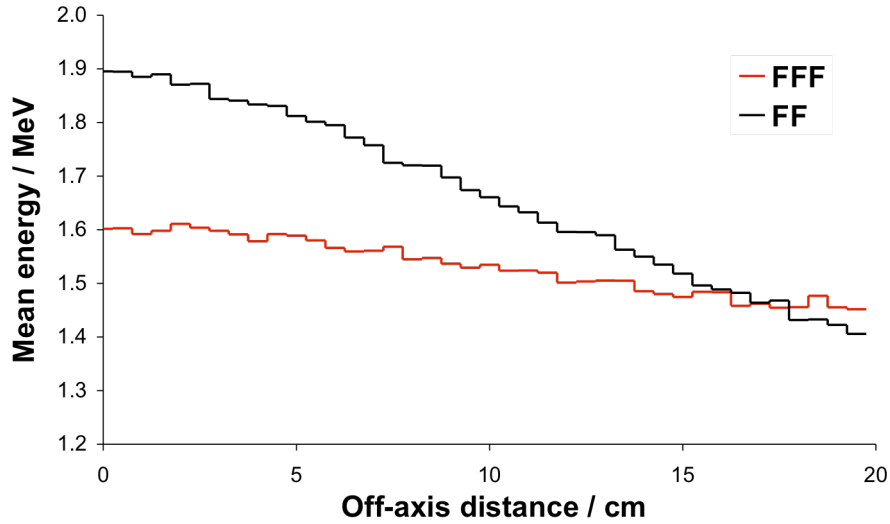


Figure A.12 Mean energy variation across the $40 \times 40 \text{ cm}^2$ field for flattened and unflattened beams free in air at a SSD of 100 cm. The estimated uncertainty is below 0.5 %.

Angular Distribution of Photons

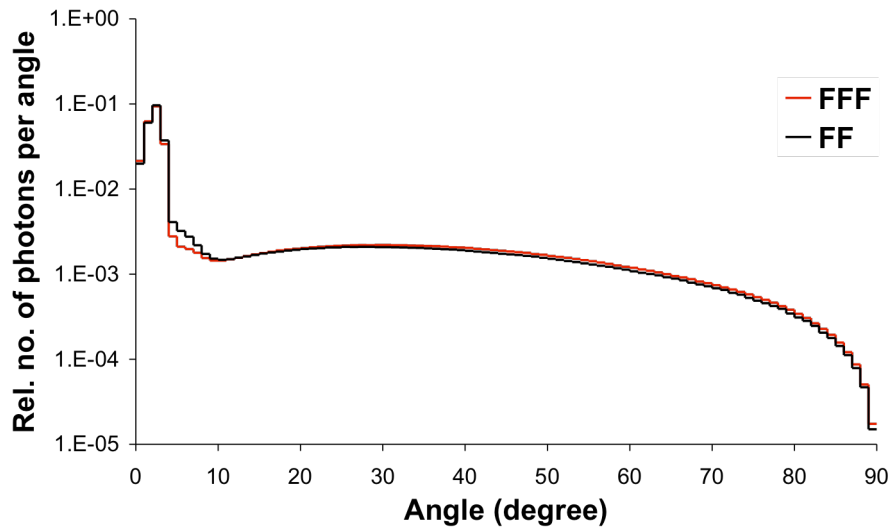


Figure A.13 Angular distribution of photons incident on the scoring plane at SSD 110 and a depth in water of 10 cm with a field size of $10 \times 10 \text{ cm}^2$. The uncertainty is below 0.5 % up to 50 degrees and below 1.2 % between 50 and 90 degrees.